Journal of Fluids and Structures 106 (2021) 103388

Contents lists available at ScienceDirect

Journal of Fluids and Structures

journal homepage: www.elsevier.com/locate/jfs

Ground effects on the propulsion of an undulating pectoral fin with various aspect ratios

Guangyu Shi [a,b,*], Qing Xiao [a], Evangelos Boulougouris [b]

[a] Department of Naval Architecture, Ocean and Marine Engineering, University of Strathclyde, Glasgow, G4 0LZ, United Kingdom
[b] Maritime Safety Research Centre, Department of Naval Architecture, Ocean and Marine Engineering, University of Strathclyde, Glasgow, G4 0LZ, United Kingdom

ARTICLE INFO

Article history:
Received 15 February 2021
Received in revised form 6 August 2021
Accepted 9 September 2021
Available online 20 September 2021

Keywords:
Undulating fin
Bio-inspired
Ground effect
Computational fluid dynamics

ABSTRACT

The propulsive performance of an undulating pectoral fin with various aspect ratios is numerically investigated with the consideration of the ground effect. The kinematics of the fin is prescribed as a sinusoidal wave and the flow field is calculated by solving the Unsteady Reynolds-Averaged Navier–Stokes equations. It is found that for higher aspect ratios, the mean thrust coefficient is linear with the square of the normalized relative velocity and the inverse square of the wavelength ratio whereas for lower aspect ratios, the relations with the velocity and wavelength become cubic and fourth power respectively. The Strouhal number is found to be a scaling parameter for longer wavelength cases. The ground effect reduces the thrust force in most cases examined in this paper while the propulsive efficiency remains relatively unchanged. Compared with the fin with longer wavelengths, the mean thrust created by the fin with a short wavelength is remarkably less influenced by the ground effect. It is believed that there is a switch from the lift-based mechanism to the added-mass mechanism as the wavelength decreases. The lift-based mechanism is the main thrust production mechanism at a longer wavelength whereas the fin with a short wavelength primarily utilizes the added-mass mechanism, i.e. is less sensitive to the change of the pressure distribution over the surface of the fin due to the ground effect.

1. Introduction

With the growing activities of ocean exploration, the need for efficient and agile autonomous underwater vehicles (AUVs) is also increasing. The performance of conventional AUVs with rotational propellers is substantially degraded at low-speed conditions (Salazar et al., 2018). Inspired by the incredible swimming performance of aquatic animals, scientists are seeking solutions from the biological diversity of the ocean. Indeed, fish exhibit a diversity of locomotion modes, which can be generally categorized into body-caudal fin (BCF) mode and median and/or paired fin (MPF) mode (Sfakiotakis et al., 1999). Although most species employ BCF modes, there are still approximately 15% of fish species utilizing MPF for swimming (Sfakiotakis et al., 1999). Among various MPF locomotion modes, the *rajiform* (e.g., manta ray and stingray) and *gymnotiform* (e.g., knifefish), which swim by undulating their expanded pectoral fins and elongated anal fins respectively, have attracted particular research interests from scientists and engineers as these two modes have the advantages of

* Corresponding author at: Department of Naval Architecture, Ocean and Marine Engineering, University of Strathclyde, Glasgow, G4 0LZ, United Kingdom.
E-mail address: guangyu.shi@strath.ac.uk (G. Shi).

https://doi.org/10.1016/j.jfluidstructs.2021.103388
0889-9746/

high maneuverability and adaptability. Some researchers have concentrated on the novel mechanical designs (Wang et al., 2015; Kim et al., 2017; Zhou and Low, 2010; Zhang et al., 2018; Low, 2009; Tangorra et al., 2007) whereas others focused on analyzing the kinematics and hydrodynamics, aiming at understanding the underlying mechanisms and optimizing for higher efficiency and maneuverability (Lauder, 2015; Taylor et al., 2013; Di Santo and Kenaley, 2016).

In the past decades, the kinematics and hydrodynamics of undulating fish fins in deep water have been investigated both experimentally (Fish et al., 2018; Rosenberger, 2001; English et al., 2019; Youngerman et al., 2014; Liu and Curet, 2017) and computationally (Dong et al., 2010; Bottom II et al., 2016; Zhang et al., 2019; Zhao and Dou, 2019). Blevins and Lauder (2012) measured the three-dimensional kinematics of the freshwater stingray (*Potamotrygon orbignyi*), which swim exclusively by generating waveforms along their enlarged pectoral fins. It was found that the wave amplitude of the fin increases in both antero-posterior and medio-lateral directions and the distal margin displayed considerable lateral curvature. Di Santo et al. (2017) studied the kinematics of the undulating pectoral fins of another species employing rajiform locomotion, the little skate *Leucoraja erinacea*. Their study emphasized on the active curvature control over the fin surface and the fin stiffening at higher swimming speed. Indeed, the benefit of actively curving fin rays was also reported in a recent numerical study of Shi et al. (2020b). With a robotic knifefish, Curet et al. (2011b) experimentally investigated the basic properties of such a biomimetic robot in self-propelled swimming. Within the parameter matrix investigated, the swimming speed of the robot increased monotonously with the augment of the sway frequency and amplitude of the fin rays. Besides, the surge force varied with frequency exponentially and the robot needed a minimum non-zero frequency to start swimming. With a similar mechanical device, Liu et al. (2017) studied the effects of ray flexibility and fin aspect ratio on the propulsion performance of the mechanical knifefish. They found that the thrust force was linear with the square of the relative velocity (between the wave speed of the fin and the incoming flow velocity) and the enclosed area swept by the fin. The power expenditure of the robot could be scaled by the cube of the effective tangential velocity of the rays. Additionally, both thrust force and power consumption declined with the increase of flexibility while the efficiency was enhanced by the optimal ray stiffness.

Computationally, Liu et al. (2015) examined the hydrodynamics of an underwater vehicle inspired by manta rays. They found that most thrust force was generated by the distal part of the fin and two sets of inter-connected vortex-rings were created behind each fin which further resulted in strong backward flow jets. Shirgaonkar et al. (2008) numerically studied the hydrodynamics of an undulating ribbon fin in calm water. The kinematics of the fin was idealized as a traveling sinusoidal wave. It was found that the fin generated both heave and surge forces and the heave force surpassed the surge force when the wavelength was decreased to two-thirds. The surge force scaled exponentially with the frequency, maximum angular deflection and aspect ratio. Curet et al. (2011a) investigated the hydrodynamic forces and the flow structures of an undulating anal fin with inward counter-propagating waves, unidirectional waves and outward counter-propagating waves. They found that compared with other types of wave forms, the inward counter-propagating wave produced a mushroom-cloud-like flow structure with an inverted jet. This downward jet created a substantial heave force, which could be utilized by aquatic animals for hovering. Neveln et al. (2014) studied the flow structures created by the undulating anal fin of knifefish both experimentally and numerically. It was observed that as the undulatory wave moves along the anal fin, a series of linked vortex tubes was shed off from the edge of the fin, which produced a jet at an oblique angle, generating both surge and heave forces simultaneously. Recently, Shi and Xiao (2021) numerically examined the propulsion performance of a biomimetic underwater robot with ray-supported undulating pectoral fins. They found that the thrust was maximized when the phase lag between the leading and trailing edge rays was 90 degrees whereas the points optimizing the efficiency varied with frequency.

Under certain circumstances, the AUVs may need to operate near the seabed, where the proximity to the ground can have considerable impact on their performance, especially those underwater vehicles inspired by rajiform swimmers such as benthic batoids and flatfishes. Therefore, it is of significance to examine the ground effect on the hydrodynamics of undulating fins. Many previous studies have been focused on investigating the dynamics of flapping foils/fins near the ground (Perkins et al., 2018; Lua et al., 2016; Fernández-prats et al., 2015). For rigid foils, Gao and Lu (2008) numerically studied the unsteady dynamics of an oscillatory foil near the ground. Three regimes of lift force behavior were identified as the foil moved away from the ground, namely, force enhancement, reduction and recovery. An experiment was carried out by Quinn et al. (2014b) to investigate the hydrodynamics of a rigid pitching foil near the ground. With the foil moving towards the solid boundary, the thrust force increased monotonically whereas the propulsion efficiency remained relatively constant. It was also observed that the lift force pulled the foil towards the ground at distances between 0.4 to 1 chord lengths while the foil was pushed away at closer proximities (0.25 to 0.4 chord lengths). Mivehchi et al. (2016) also experimentally studied the ground effect experienced by a rigid flapping foil. Similar to Quinn et al. (2014b), for almost all the cases under consideration, the thrust of the foil near the ground was improved while the propulsion efficiency varied within a small range. It was also suggested that the instantaneous force profiles could change significantly without altering the mean force values, i.e., the mean force measurement alone is not sufficient to indicate the proximity effect of the solid wall.

In terms of flexible foils/fins in ground effect, Quinn et al. (2014a) conducted an experimental study on the potential hydrodynamic benefits of a flexible plate swimming near a solid boundary and found that the plate had higher swimming speed near the ground whereas the swimming efficiency remained constant for most cases except those near the resonance condition of the plate where the efficiency was enhanced. Computationally, Park et al. (2017) studied the free locomotion of a two-dimensional flexible fin near a solid wall. It was found that the swimming speed and propulsive

Table 1
Summary of the parameters investigated in the present study.

AR	*D/H*	λ/L	f_r
0.5	$+\infty$, 10, 5, 2.5	1, 2, 3, 4	0.5∼4.0
0.25	$+\infty$, 10, 5, 2.5	1, 2, 3, 4	1.0∼4.0
0.125	$+\infty$, 10, 5, 2.5	1, 2, 3, 4	2.0∼4.0

efficiency of the fin could be increased by 14% and 17% respectively when flapping near the ground. Besides, the kinematics of the fin was altered passively near the solid boundary, which indirectly resulted in the benefits or penalties of the ground effect. The enhanced swimming speed and propulsive efficiency in ground proximity were also reported by Dai et al. (2016) and Zhang et al. (2017). However, the ground effect is not necessarily beneficial to fish locomotion. Blevins and Lauder (2013) experimentally investigated the swimming performance of a very flexible heave panel near the ground and found that under most kinematics, the fin did not swim faster near the ground and the power consumption was increased. Indeed, Quinn et al. (2014a) also reported that the benefits from the ground effect were restricted to certain frequency ranges, indicating that benthic fish may modulate their kinematics to obtain benefits from the ground effect. Furthermore, in these studies of flexible foils (Quinn et al., 2014a; Park et al., 2017; Dai et al., 2016; Zhang et al., 2017), the foil's deformation was mainly limited to the first bending mode whereas in the experiment of Blevins and Lauder (2013), the foil experienced significant higher bending modes, implying the importance of the exact kinematics and deformation pattern.

Despite the extensive study on the fluid dynamics of undulating fins and the ground effect on both rigid and flexible flapping foils/fins, the hydrodynamics of an undulating pectoral fin near the ground has not been fully examined and understood. The kinematics and deformation of an undulatory pectoral fin are significantly different from those of a flapping foil, thus the previous findings from flapping foils in ground effect may not apply to undulating fins. Moreover, an enhanced understanding on the hydrodynamics of undulatory pectoral fins in ground proximity could aid the design and control of underwater vehicles inspired by rajiform swimmers. Bearing this in mind, in the present study, we numerically investigate propulsive performance of a three-dimensional undulating pectoral fin with various aspect ratios in the presence and absence of the ground effect. The kinematics of the fin is prescribed as a sinusoidal traveling wave and the fluid dynamics is simulated by solving Unsteady Reynolds-Averaged Navier–Stokes equations (URANS). The objectives of the present study are to investigate how the force generation and propulsive efficiency of an undulatory pectoral fin vary with the aspect ratio and ground proximity. We are also aiming at providing some useful guidelines for the design and control of biomimetic underwater vehicles, especially when operating near the substrate.

The rest of this paper is organized as follows: in Section 2, the dimensions and kinematics of the fin are described. In Section 3, the governing equations, numerical methods and the validation of the flow solver are presented. In Section 4, the numerical results, including the force generation, propulsive efficiency and near-fin flow field are analyzed. The conclusions are drawn in the final section.

2. Problem description

In the present study, we numerically examine the hydrodynamics of an undulating pectoral fin near the ground. As illustrated in Fig. 1(a), the pectoral fin is placed in a flow with an incoming velocity U_∞ and its position in x-direction is fixed, i.e., the fin is not swimming freely. Fig. 1(b–d) demonstrate the side, top and front views of the fin and its key dimensions. The pectoral fin has a length of L and a width of W, and its aspect ratio is defined as $AR = W/L$. The Reynolds number based on L and U_∞ is $Re = 1 \times 10^4$. The distance of the fin's horizontal plane (x-z plane) to the ground is denoted by D. The motion of the fin is prescribed as a traveling wave along x-direction, i.e., each point on the fin performs a rolling motion around x-axis as shown in Fig. 1(a). The kinematics of the fin is modeled as a traveling sinusoidal wave, which can be mathematically formulated as

$$\theta(x,t) = \theta_0 sin\left[2\pi\left(f \cdot t - \frac{x}{\lambda}\right)\right], \tag{1}$$

where θ_0 is the maximum angular deflection of the fin from the horizontal plane, λ is the wavelength, f is the motion frequency, t is time and x is the coordinate in axial-direction. Here, θ_0 is chosen to be 30 degrees. Correspondingly, the maximum deflection amplitude is $H = Wsin(\theta_0) = 0.5W$. The reduced frequency is defined as $f_r = \frac{fL}{U_\infty}$ and the Strouhal number is $S_t = \frac{fH}{U_\infty}$, which is defined based on the amplitude of the mid-point of the leading edge. In the present work, three aspect ratios (AR = 0.5, 0.25 and 0.125), four wavelength ratios (λ/L = 1, 2, 3 and 4) and four depth values (D/H = 2.5, 5.0, 10.0 and $+\infty$) are considered. Table 1 summarizes the parameters simulated in the current study. It should be noted that all parameters in the present paper are non-dimensional (e.g., Reynolds number, reduced frequency and aspect ratio), thus no absolute values are provided.

The hydrodynamic performance of the pectoral fin is characterized by the time-averaged thrust coefficient $\overline{C_T}$ and vertical force coefficient $\overline{C_Y}$, the amplitude of the vertical force coefficient $\widetilde{C_Y}$ and the propulsive efficiency η. The

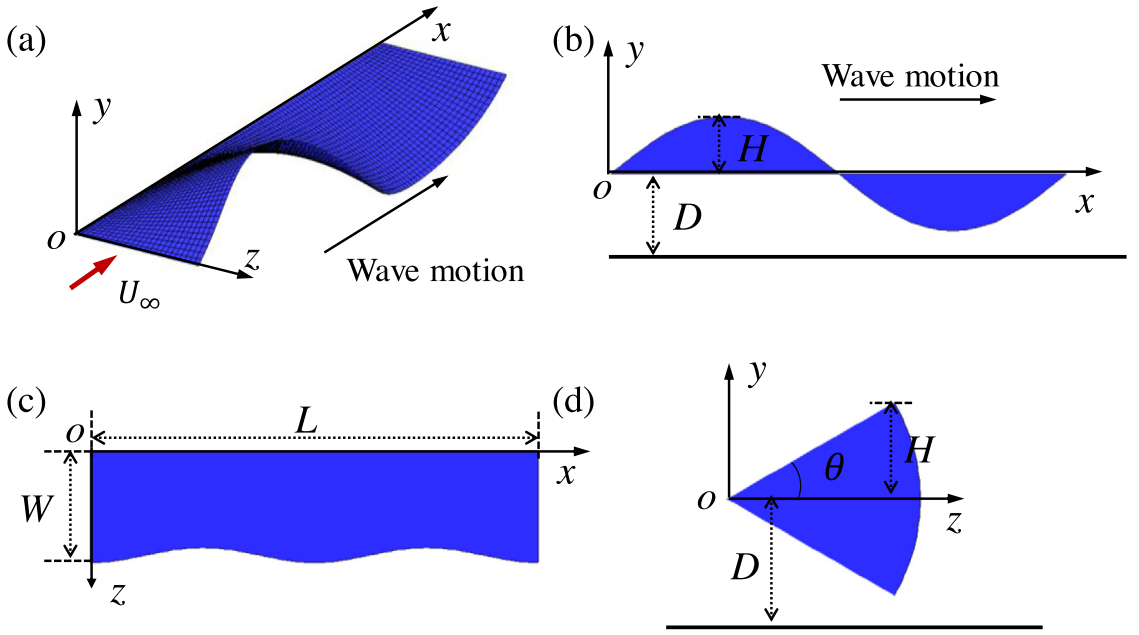

Fig. 1. Schematic views of the undulating pectoral fin. (a) 3D view, (b) side view, (c) top view, and (d) front view.

instantaneous thrust coefficient C_T, vertical force coefficient C_Y and power expenditure coefficient C_P are defined as

$$\begin{aligned} C_T &= \frac{-F_X(t)}{0.5\rho U_\infty^2 S_e} \\ C_Y &= \frac{F_Y(t)}{0.5\rho U_\infty^2 S_e}, \\ C_P &= \frac{P(t)}{0.5\rho U_\infty^3 S_e} \end{aligned} \tag{2}$$

where $F_X(t)$ and $F_Y(t)$ are the x- and y-component of the fluid force acting on the surface of the fin respectively. S_e is the enclosed area, which can be calculated as $S_e = 2HL = WL$. A negative sign is included in the definition of the thrust coefficient because it is in the opposite direction of x-axis and wave propagation. $P(t)$ is the instantaneous power expenditure, which is evaluated as (Dai et al., 2012):

$$P(t) = \iint_S -\mathbf{F}(\mathbf{x}, t) \cdot \boldsymbol{v}_{\text{fin}}(\mathbf{x}, t)\, d\mathbf{x}, \tag{3}$$

where $\boldsymbol{v}_{\text{fin}}(\mathbf{x}, t)$ is the local moving velocity of the fin. $\overline{C_T}$, $\overline{C_Y}$ and $\overline{C_P}$ are averaged over one motion period after reaching the periodical stage whereas $\widetilde{C_Y}$ is calculated by averaging the absolute values of the maxima and minima of C_Y within one motion period:

$$\widetilde{C_Y} = \frac{|max\{C_Y\}| + |min\{C_Y\}|}{2}. \tag{4}$$

Finally, the propulsive efficiency is defined as:

$$\eta = \frac{-\overline{F}_X U_\infty}{\overline{P}} = \frac{\overline{C}_T}{\overline{C}_P}. \tag{5}$$

3. Computational fluid dynamics

3.1. Mathematical formulation

In the present work, the flow field is resolved by solving the compressible Unsteady Reynolds-Averaged Navier–Stokes (URANS) equations using a finite volume method. The flow governing equations can be expressed in its integral form as follows (Liu and Ji, 1996):

$$\frac{\partial}{\partial t}\iiint_V \mathbf{Q}\, dV + \iint_S \boldsymbol{G_c} \cdot \boldsymbol{n} dS - \iint_S \boldsymbol{G_v} \cdot \boldsymbol{n} dS = \iiint_V \hat{\boldsymbol{S}} dV, \tag{6}$$

where $\boldsymbol{Q} = (\rho, \rho\boldsymbol{v}, \rho E, \rho k, \rho\omega)^T$ is the conservative variable vector, t is time, V is the control volume , S is the boundary surface enclosing the volume, and $\boldsymbol{n}$ is the surface unit normal vector in outward direction. ρ is the fluid density, $\boldsymbol{v}$ is the flow velocity vector and E is the total energy. k and ω are the turbulent kinetic energy and the specific dissipation rate respectively. $\boldsymbol{G_c}$ and $\boldsymbol{G_v}$ are the convective and diffusive flux vectors, which can be expressed as

$$\boldsymbol{G_c} = \begin{bmatrix} \rho\tilde{\boldsymbol{v}}^T \\ \rho\tilde{\boldsymbol{v}}\boldsymbol{v} + p\boldsymbol{I} \\ (\rho E\tilde{\boldsymbol{v}} + p\boldsymbol{v})^T \\ \rho k\tilde{\boldsymbol{v}}^T \\ \rho\omega\tilde{\boldsymbol{v}}^T \end{bmatrix}, \tag{7}$$

where $\tilde{\boldsymbol{v}}$ is the relative velocity vector, defined as $\tilde{\boldsymbol{v}} = \boldsymbol{v} - \boldsymbol{v_g}$, and $\boldsymbol{v_g}$ is the grid velocity vector, and p is the pressure.

$$\boldsymbol{G_v} = \begin{bmatrix} 0 \\ \boldsymbol{\tau} \\ \left(\boldsymbol{\tau}\cdot\boldsymbol{v} + (\mu + \sigma_k\mu_t)\dfrac{\partial k}{\partial \boldsymbol{x}} - \boldsymbol{q}\right)^T \\ (\mu + \sigma_k\mu_t)\dfrac{\partial k}{\partial \boldsymbol{x}} \\ (\mu + \sigma_\omega\mu_t)\dfrac{\partial \omega}{\partial \boldsymbol{x}} \end{bmatrix}. \tag{8}$$

$\hat{\boldsymbol{S}}$ is the source term of k-ω turbulence model, which is formulated as (Liu and Ji, 1996)

$$\hat{\boldsymbol{S}} = \begin{bmatrix} 0 \\ 0 \\ 0 \\ \hat{\tau}_{ij}\dfrac{\partial v_i}{\partial x_j} - \beta^*\rho\omega k \\ \dfrac{\alpha\omega}{k}\hat{\tau}_{ij}\dfrac{\partial v_i}{\partial x_j} - \beta\rho\omega^2 \end{bmatrix}. \tag{9}$$

In Eqs. (8) and (9), $\boldsymbol{x} = (x, y, z)$ is the position vector and x_i or x_j is its component. Similarly, v_i or v_j denotes the component of flow velocity vector $\boldsymbol{v}$. Additionally,

$$\mu_t = \alpha^*\left(\frac{\rho k}{\omega}\right), \tag{10}$$

$$\chi_{ij} = \frac{1}{2}\left(\frac{\partial v_i}{\partial x_j} + \frac{\partial v_j}{\partial x_i}\right) - \frac{1}{3}(\nabla\cdot\boldsymbol{v})\,\delta_{ij}, \tag{11}$$

$$\hat{\tau}_{ij} = 2\mu_t\chi_{ij} - \frac{2}{3}\rho k\delta_{ij}, \tag{12}$$

$$\tau_{ij} = 2\mu\chi_{ij} + \hat{\tau}_{ij}, \tag{13}$$

$$q_j = -\left(\frac{\mu}{Pr_L} + \frac{\mu_t}{Pr_T}\right)\frac{\partial h}{\partial x_j}, \tag{14}$$

where μ and μ_t are the laminar and turbulent eddy viscosity, respectively. $Pr_L = 0.712$ and $Pr_T = 0.9$ are the laminar and turbulent Prandtl numbers respectively. $h = e + p/\rho$ is the flow enthalpy and $e = p/[(\gamma - 1)\rho]$ is the flow internal energy, where $\gamma = 1.4$ is the ratio of specific heats. The other closure constants are (Liu and Ji, 1996):

$$\begin{aligned} &\sigma_k = \frac{1}{2}, \quad \sigma_\omega = \frac{1}{2}, \quad \beta^* = \frac{9}{100} \\ &\beta = \frac{3}{40}, \quad \alpha = \frac{5}{9}, \quad \alpha^* = 1 \end{aligned}. \tag{15}$$

3.2. Numerical schemes

The fluid equation Eq. (6) is discretized by a cell-centered finite volume method based on a multi-block, structured grid system (Shi et al., 2019; Liao et al., 2007). With a structured grid method, the fluid domain is divided into an array of hexahedral cells. Each grid cell is uniquely denoted by three indices i, j, k. For each hexahedral cell (i, j, k), the conservation laws are applied and the following semi-discrete form can be derived:

$$\frac{\partial}{\partial t}\left(\boldsymbol{Q}_{i,j,k}\Delta V_{i,j,k}\right) - \boldsymbol{F}_{i,j,k} = \boldsymbol{A}_{i,j,k}, \tag{16}$$

where $\boldsymbol{F}_{i,j,k}$ is the total convective and diffusive fluxes going through the six faces of the hexahedral cell. $\boldsymbol{A}_{i,j,k}$ denotes the artificial dissipation, which is used for numerical stability (Jameson et al., 1981).

For unsteady flows, the dual-time stepping algorithm (Jameson, 1991) is employed for the temporal integration, where Eq. (16) is reformulated as a steady-state problem with a pseudo-time $\tilde{t}$:

$$\frac{\partial}{\partial \tilde{t}}\boldsymbol{Q}^{n+1} = \frac{1}{\Delta V^{n+1}}\tilde{\boldsymbol{F}}\left(\boldsymbol{Q}^{n+1}\right), \tag{17}$$

where

$$\tilde{\boldsymbol{F}}\left(\boldsymbol{Q}^{n+1}\right) = \boldsymbol{F}\left(\boldsymbol{Q}^{n+1}\right) + \boldsymbol{A}\left(\boldsymbol{Q}^{n+1}\right) - \frac{3\left(\boldsymbol{Q}\Delta V\right)^{n+1} - 4\left(\boldsymbol{Q}\Delta V\right)^{n} + \left(\boldsymbol{Q}\Delta V\right)^{n-1}}{2\Delta t}. \tag{18}$$

Eq. (17) is then integrated by a hybrid multistage Runge–Kutta scheme (Jameson, 1991). For l-stages, the Runge–Kutta scheme can be expressed as

$$\begin{aligned}
\boldsymbol{Q}_{i,j,k}^{(0)} &= \boldsymbol{Q}_{i,j,k}^{n} \\
\boldsymbol{Q}_{i,j,k}^{(1)} &= \boldsymbol{Q}_{i,j,k}^{(0)} + \alpha_1 \frac{\Delta\tilde{t}_{i,j,k}}{\Delta V_{i,j,k}^{n+1}}\tilde{\boldsymbol{F}}^{(0)} \\
&\cdots \\
\boldsymbol{Q}_{i,j,k}^{(l)} &= \boldsymbol{Q}_{i,j,k}^{(0)} + \alpha_l \frac{\Delta\tilde{t}_{i,j,k}}{\Delta V_{i,j,k}^{n+1}}\tilde{\boldsymbol{F}}^{(l-1)} \\
\boldsymbol{Q}_{i,j,k}^{n+1} &= \boldsymbol{Q}_{i,j,k}^{(l)}
\end{aligned} \tag{19}$$

where α_l is the coefficient for stage l and $\Delta\tilde{t}_{i,j,k}$ is the local time step for cell (i, j, k).

The mesh deformation is handled by a fast and robust moving mesh algorithm, which combines a spring-analogy method and the trans-finite interpolation (Tsai et al., 2001). It should also be noted that a compressible flow solver was used in the present research, it is therefore important to minimize the compressibility effect. As no preconditioning methods are implemented in the current flow solver, the freestream Mach number (defined as $Ma_\infty = U_\infty/a$, where a is the speed of sound) should be kept as low as possible. Here, the freestream Mach number was set to be 0.06, which is the lowest value the present flow solver can reach while keeping the numerical stability and accuracy.

3.3. Numerical validation

The present flow solver has been extensively validated and applied to investigate the tidal turbine and biomimetic propulsion in previous publications (Shi et al., 2019; Xiao and Liao, 2010; Liu et al., 2016; Liu and Xiao, 2015; Luo et al., 2020). Here, it is further validated by evaluating the fluid dynamics of an oscillating hydrofoil at $Re = 5 \times 10^5$ (Kinsey and Dumas, 2012). The hydrofoil (chord length c) undergoes a combined heave and pitch motion:

$$\begin{aligned}
\overline{\theta}(t) &= \overline{\theta}_0 sin(\overline{\omega}t) \\
\overline{h}(t) &= \overline{h}_0 sin(\overline{\omega}t + \overline{\varphi})
\end{aligned}, \tag{20}$$

where $\overline{h}_0 = c$, $\overline{\theta}_0 = 75°$ and $\overline{\varphi} = 90°$. The pitching point is located at the 1/3 chord length from the leading edge and the reduced frequency is defined as $f^* = \overline{\omega}c/2\pi U_\infty$. Fig. 2 (a–c) demonstrate the comparison of the instantaneous force and power coefficients at $f^* = 0.14$ between the present result and the data of Kinsey and Dumas (2012). It is observed that the current simulation results agree well with those from literature. Besides, the presently computed energy extraction efficiency is also in good agreement with that in Ref. Kinsey and Dumas (2012), as shown in Fig. 2(d).

4. Results and discussions

The problem depicted in Section 2 is resolved using the numerical methods presented in Section 3. The dimensions of the computational domain and corresponding boundary conditions are illustrated in Fig. 3(a). The fin is modeled as an infinite thin membrane where the no-slip wall boundary condition is applied. The symmetry boundary condition is used for the x-y plane. The bottom domain boundary is regarded as a no-slip wall if the ground effect is considered. Otherwise, the bottom and the rest domain boundaries are taken as far-fields, where a non-reflective far-field boundary condition is applied. Fig. 3(b) shows the computational mesh used in the present study, where a body-fitted structured mesh is generated discretizing the computational domain into hexahedral cells. The region near the fin surface is refined in order to capture the flow boundary layer. The distance of the first grid layer to the fin surface is determined by setting $y+ = 1.0$.

A sensitivity study with respect to the mesh density and time-step is carried out in order to verify the flow mesh size and physical time-step used in the present work. Three different grid densities and time-steps are used and the corresponding time-averaged thrust coefficients are detailed in Table 2, where N_{cd} and N_{sp} are the number of mesh cells in the chordwise and spanwise directions of the fin. The results are also demonstrated in Fig. 4, from which we can observe that with the refinements of the flow mesh and physical time-step, the numerical results have reached convergence. Based on this sensitivity study, Mesh_M and $dt = T/120$ are used in the following simulations.

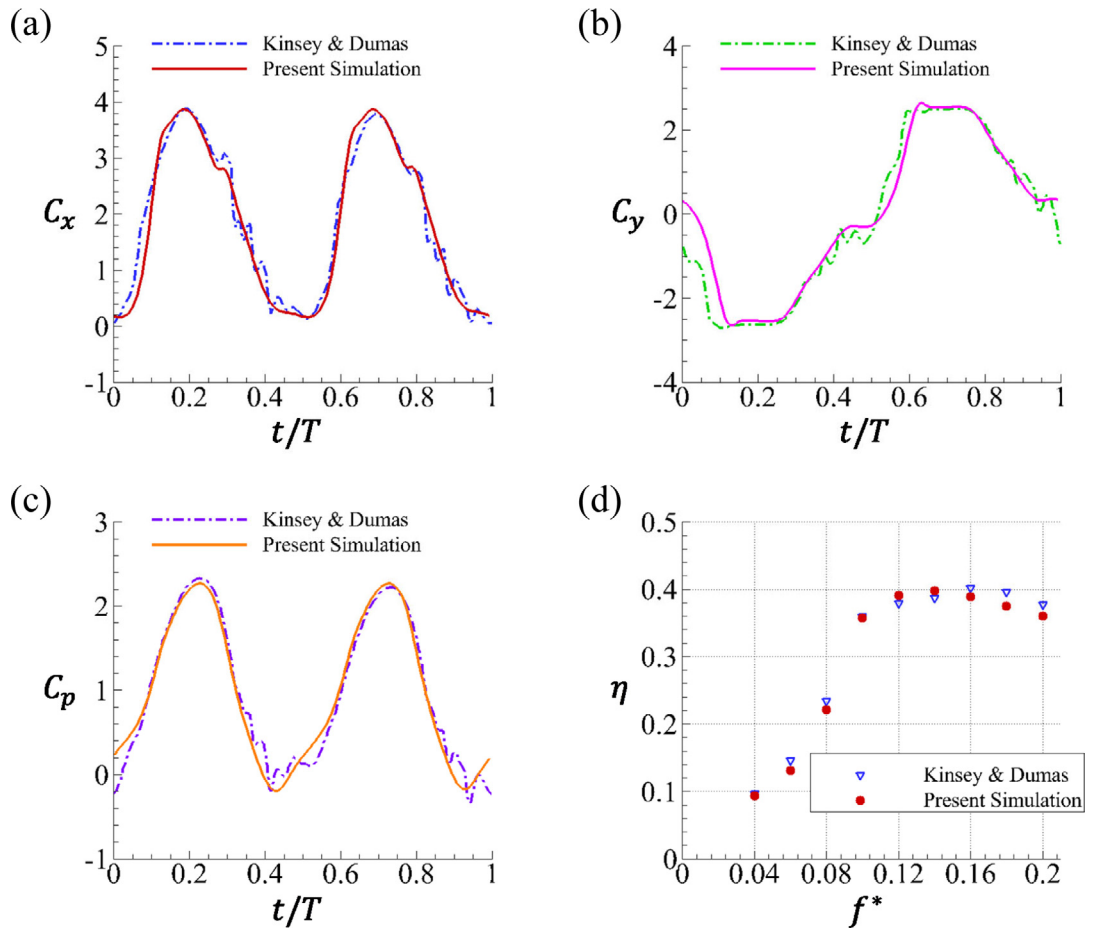

Fig. 2. The instantaneous force (a, b) and power (c) coefficients at $f^* = 0.14$. Subplot (d) shows the energy extraction efficiency as a function of reduced frequency (Kinsey and Dumas, 2012). The k-ω turbulent model was used in both studies.

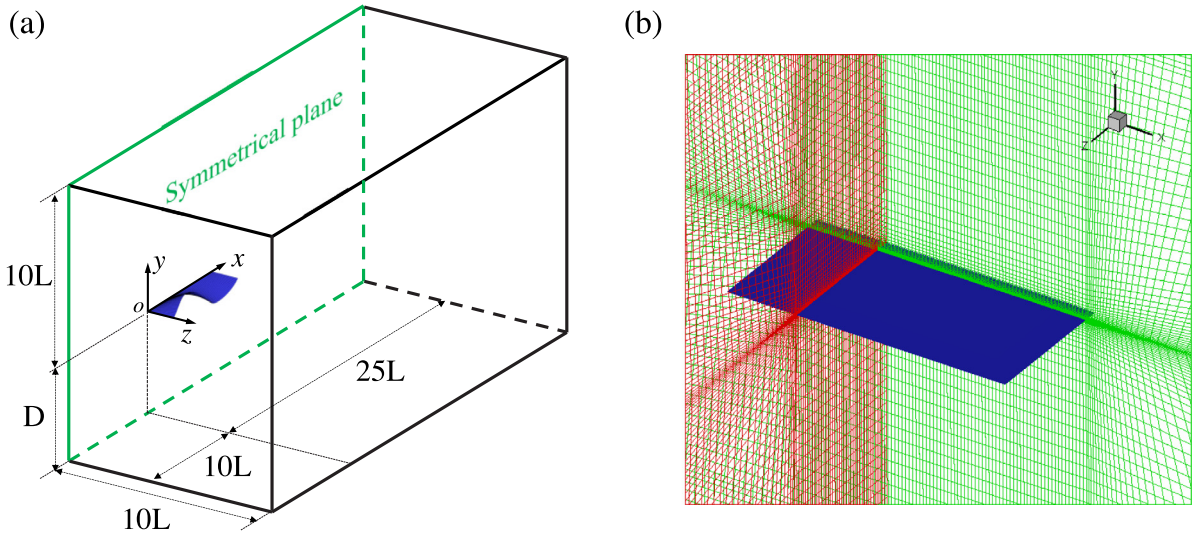

Fig. 3. Computational domain (a) and mesh (b) used in the present study.

Table 2
Thrust coefficients of different mesh densities and time steps.

	Mesh size	N_{cd}	N_{sp}	dt/T	$\overline{C_T}$
Mesh_F	9.0 Million	100	60	1/120	5.13
Mesh_C	3.6 Million	64	40	1/120	5.09
Mesh_M	5.8 Million	80	40	1/120	5.06
Mesh_M	5.8 Million	80	40	1/160	5.08
Mesh_M	5.8 Million	80	40	1/80	5.03

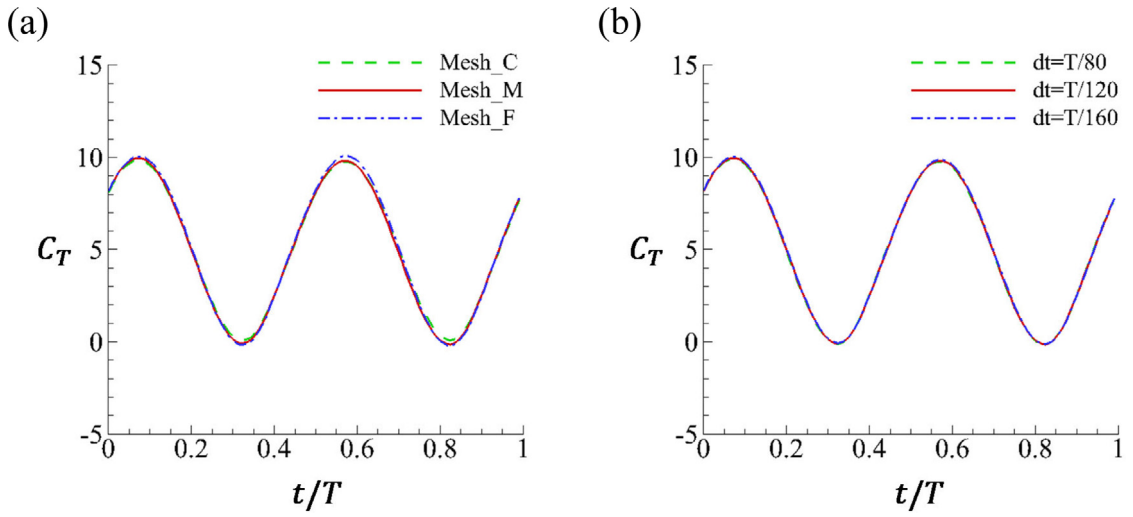

Fig. 4. Sensitivity study of the present CFD code to (a) mesh density ($dt = T/120$) and (b) physical time step (Mesh_M).

4.1. Propulsive performance at various aspect ratios

In this section, the hydrodynamic forces and propulsive efficiency generated by the undulating fin without the ground effect are firstly presented and discussed.

4.1.1. Hydrodynamic forces

The variations of the time-averaged thrust coefficients ($\overline{C_T}$) and amplitudes of vertical force coefficients ($\widetilde{C_Y}$) with respect to reduced frequency are shown in Fig. 5. It is obvious that for all the wavelengths and aspect ratios considered here, both thrust force and vertical force amplitude increase exponentially with the reduced frequency (f_r), which agrees with the finding of Shirgaonkar et al. (2008). A closer inspection on the time-averaged thrust coefficients at three different aspect ratios (Fig. 5(a–c)) reveals that at smaller aspect ratios (e.g., AR = 0.125), the fin with shorter wavelengths (e.g., $\lambda/L = 1.0$) creates larger thrust forces. In terms of the amplitudes of the vertical force coefficient, it is observed that for all three aspect ratios, longer wavelengths produce higher vertical force amplitudes. Moreover, the vertical force amplitudes at $\lambda/L = 1.0$ are substantially smaller than those of the other wavelength values, indicating the energy consumption at $\lambda/L = 1.0$ will be significantly lower.

The time-averaged thrust coefficients ($\overline{C_T}$) and amplitudes of vertical force coefficients ($\widetilde{C_Y}$) as functions of Strouhal number (S_t) are plotted in Fig. 6. It is observed that for shorter wavelengths, the $\overline{C_T}$ data from different aspect ratios are scattered. However, for the case of $\lambda/L = 4.0$, the Strouhal number collapses the mean thrust coefficients remarkably well for all three aspect ratios examined here, as shown in Fig. 6(c). This is reminiscent of previous research on flexible flapping foils (Heathcote et al., 2008), where the thrust and power-input coefficients at various flexibilities were collapsed when plotted against Strouhal number. Indeed, for the case of $\lambda/L = 4.0$, the motion of the fin is often considered as flapping rather than undulating ($\lambda/L \leq 1.0$). Therefore, it is not surprising that the Strouhal number can be a scaling parameter characterizing the thrust production of the pectoral fin at $\lambda/L = 4.0$.

As discussed by Liu et al. (2017), the thrust force generated by an undulating anal fin was approximately linear with the square of the relative velocity between the traveling wave and the incoming flow, and the enclosed area swept by the fin, i.e.,

$$\overline{F_T} \sim V_r^2 S_e, \tag{21}$$

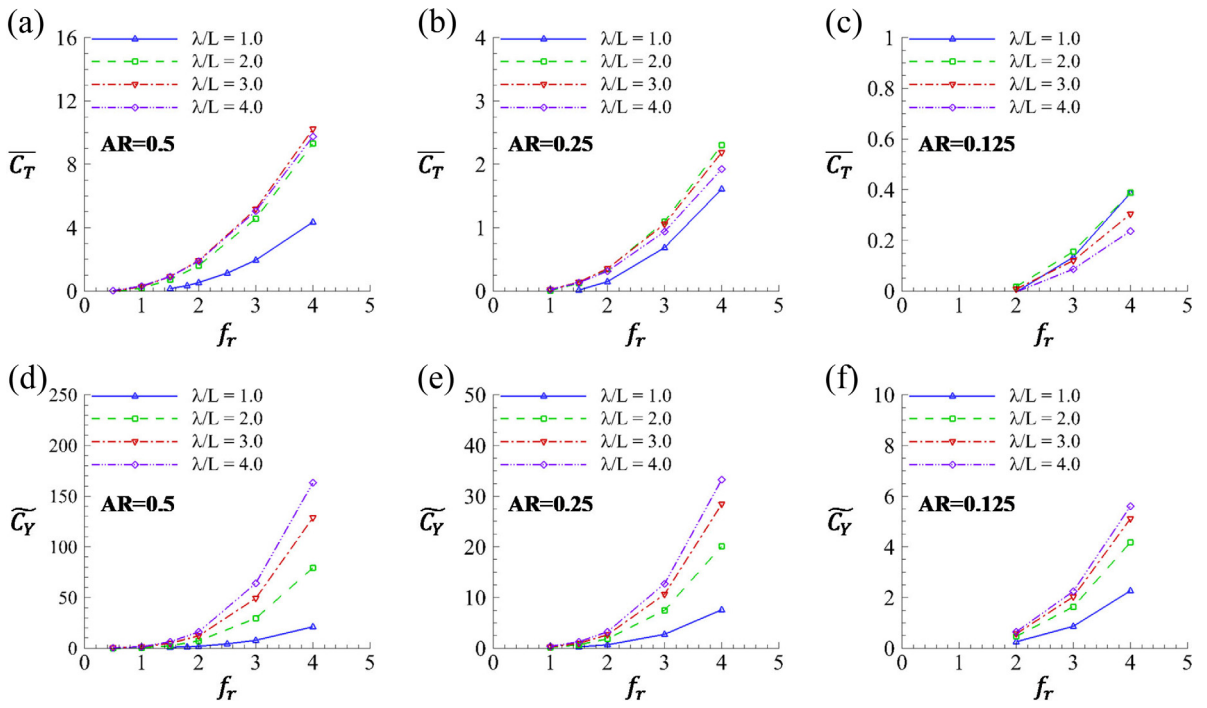

Fig. 5. Mean thrust coefficients (a–c) and amplitudes of vertical force coefficients (d–f) as functions of reduced frequency at various wavelengths and aspect ratios. (a,d) $AR = 0.5$, and (b,e) $AR = 0.25$, and (c,f) $AR = 0.125$.

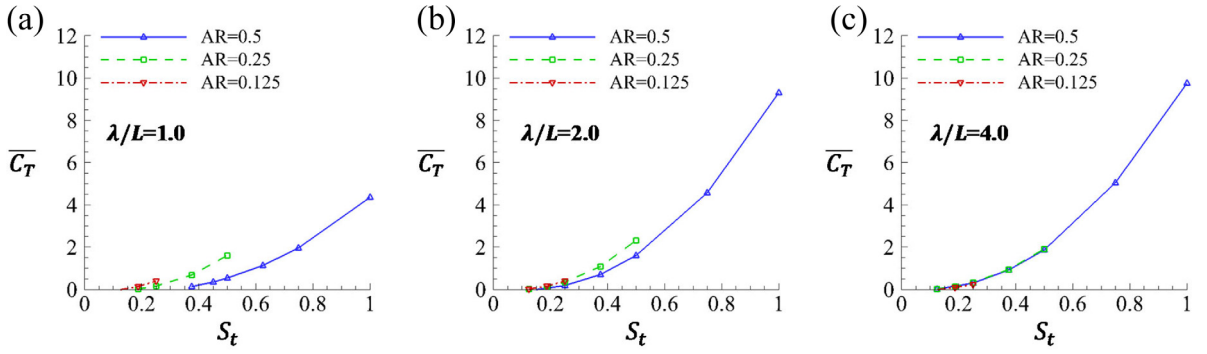

Fig. 6. Mean thrust coefficients as functions of Strouhal number at various wavelengths and aspect ratios. (a) $\lambda/L = 1.0$, and (b) $\lambda/L = 2.0$, and (c) $\lambda/L = 4.0$.

where $V_r = f\lambda - U_\infty$ and $\overline{F_T}$ is the mean thrust force. Thus, we have

$$\frac{\overline{F_T}}{0.5\rho U_\infty^2 S_e} \sim \frac{V_r^2}{U_\infty^2}, \tag{22}$$

and then

$$\overline{C_T} \sim V_{rel}^2, \tag{23}$$

where $V_{rel} = V_r/U_\infty$ is the normalized relative velocity between the traveling wave and the incoming flow. Therefore, the mean thrust coefficient is linear with the square of the normalized relative velocity. Considering the effect of wavelength, we propose the following relation between $\overline{C_T}$ and V_{rel} and λ/L.

$$\overline{C_T} \sim \gamma_t V_{rel}^{\alpha_t} (\lambda/L)^{\beta_t}. \tag{24}$$

Similarly,

$$\widetilde{C_Y} \sim \gamma_v V_{rel}^{\alpha_v} (\lambda/L)^{\beta_v}. \tag{25}$$

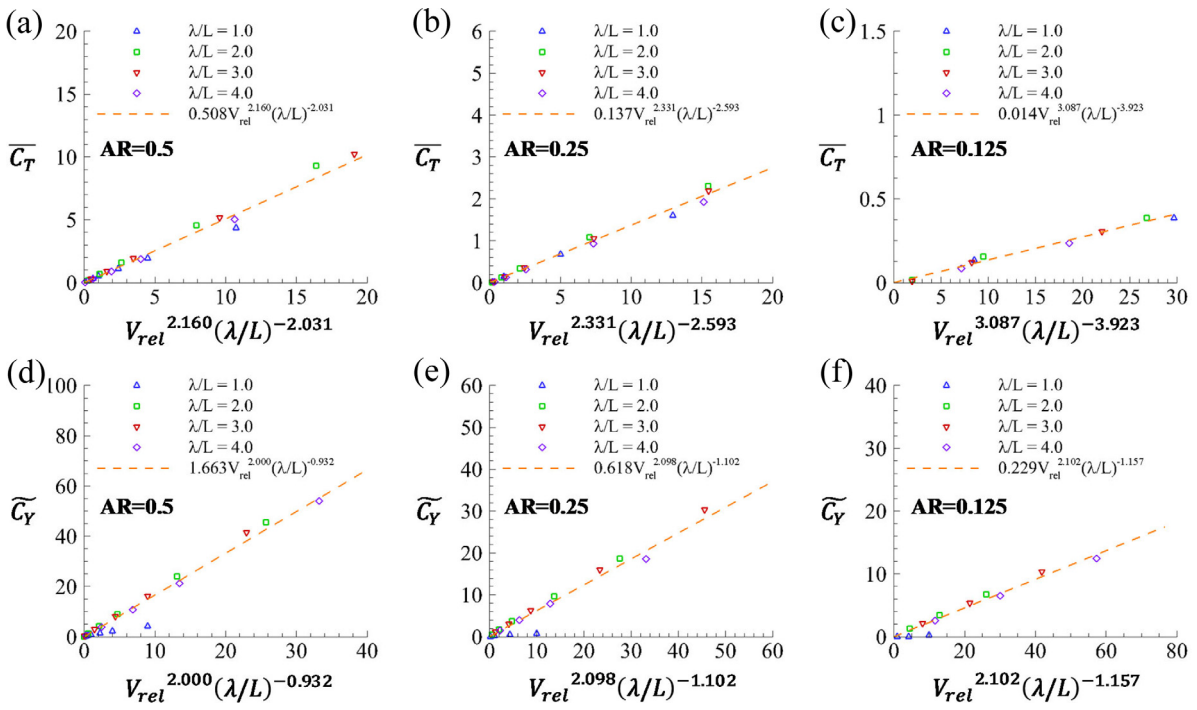

Fig. 7. The scaling laws of the mean thrust coefficients (a–c) and amplitudes of vertical force coefficients (d–f) in terms of new parameters combining relative velocity (V_{rel}) and wavelength (λ/L). (a,d) $AR = 0.5$, and (b,e) $AR = 0.25$, and (c,f) $AR = 0.125$.

Table 3
Summary of data fitting parameters for various aspect ratios.

	$\overline{C_T}$			$\widetilde{C_Y}$		
	γ_t	α_t	β_t	γ_v	α_v	β_v
AR = 0.5	0.508	2.160	−2.031	1.663	2.000	−0.932
AR = 0.25	0.137	2.331	−2.593	0.618	2.098	−1.102
AR = 0.125	0.014	3.087	−3.923	0.229	2.102	−1.157

The data fitting results are demonstrated in Fig. 7 and the values of those coefficients are tabulated in Table 3. It is observed that for the thrust coefficient, α_t is between 2.160 and 3.087 while β_t ranges from −3.923 to −2.031. Therefore, in general, the thrust coefficient of an undulating pectoral fin is linear with the square (higher AR) or cube (lower AR) of the normalized relative velocity (V_{rel}) and the inverse of the square (high AR) or the fourth power (low AR) of the wavelength ratio (λ/L). Similarly, the vertical force coefficient is linear with the square of the normalized relative velocity and the inverse of the wavelength ratio. A closer inspection of Fig. 7(d–f) reveals that the amplitudes of the vertical force coefficient ($\widetilde{C_Y}$) at $\lambda/L = 1.0$ are considerably below the fitted line, implying existence of significant differences between the case of $\lambda/L = 1.0$ and the others, which will be discussed later.

Fig. 8 shows the time histories of the thrust coefficients at different wavelengths and aspect ratios. For all cases presented in here, two thrust peaks and two troughs are created within one motion cycle. For the same wavelength, the profiles of the thrust between various aspect ratios and reduced frequencies are similar. The main difference is that as the reduction of aspect ratio and reduced frequency, the magnitudes of the thrust decrease as well. When $\lambda/L = 1.0$, both the thrust peaks and troughs increase with the reduced frequency. In contrast, at $\lambda/L = 4.0$, the thrust peaks rise significantly whereas the troughs only change slightly and stay close to zero. This phenomenon is associated with different deformations and propulsive mechanisms employed by the fin at $\lambda/L = 1.0$ and 4.0, which will be discussed in detail in Section 4.4.2. Besides, for both wavelengths presented in Fig. 8, the phase shifts are marginal as the increase of the reduced frequency. Fig. 9 illustrates the instantaneous vertical force coefficients within one motion cycle at different wavelengths and aspect ratios. It is seen that for all cases presented here, as the motion frequency increases, the amplitudes of the vertical force increase as well. The profiles of the vertical force at different aspect ratios and frequencies can be well fitted using harmonic functions.

4.1.2. Propulsive efficiency

Fig. 10 demonstrates the propulsive efficiency as functions of motion frequency at different wavelengths and aspect ratios. It can be seen that the propulsive efficiency rises with the increase of the reduced frequency first and then declines

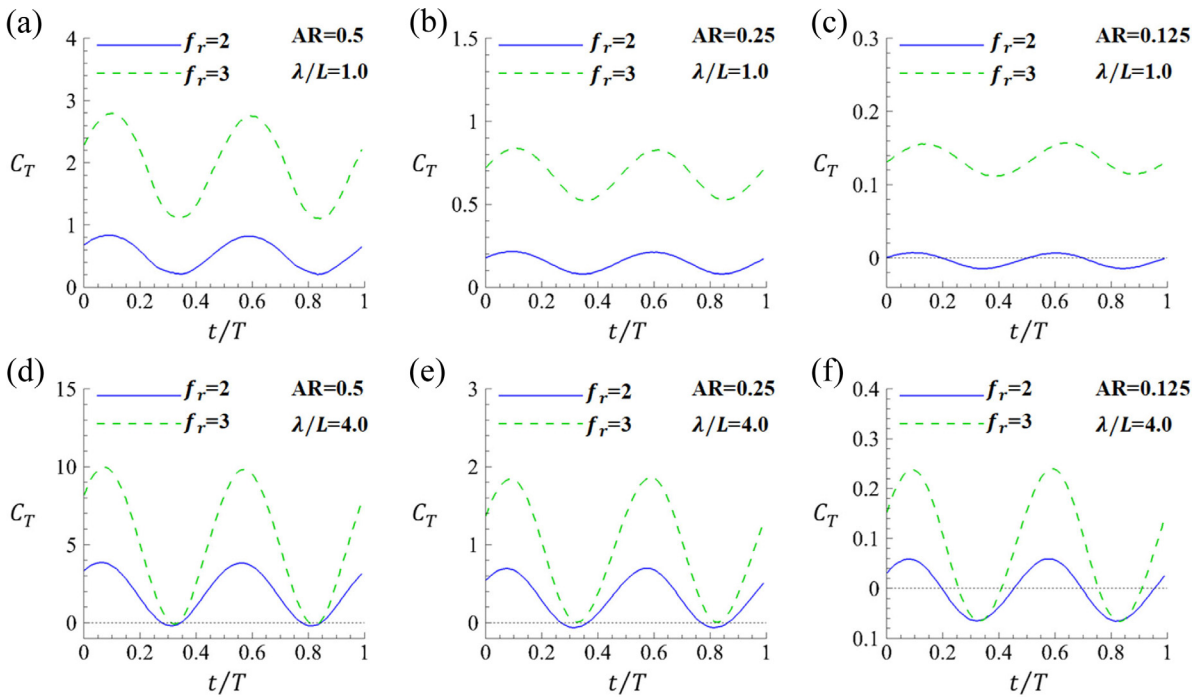

Fig. 8. Instantaneous thrust coefficients within one motion period at various motion frequencies. (a–c) $\lambda/L = 1.0$, and (d–f) $\lambda/L = 4.0$. (a,d) $AR = 0.5$, and (b,e) $AR = 0.25$, and (c,f) $AR = 0.125$.

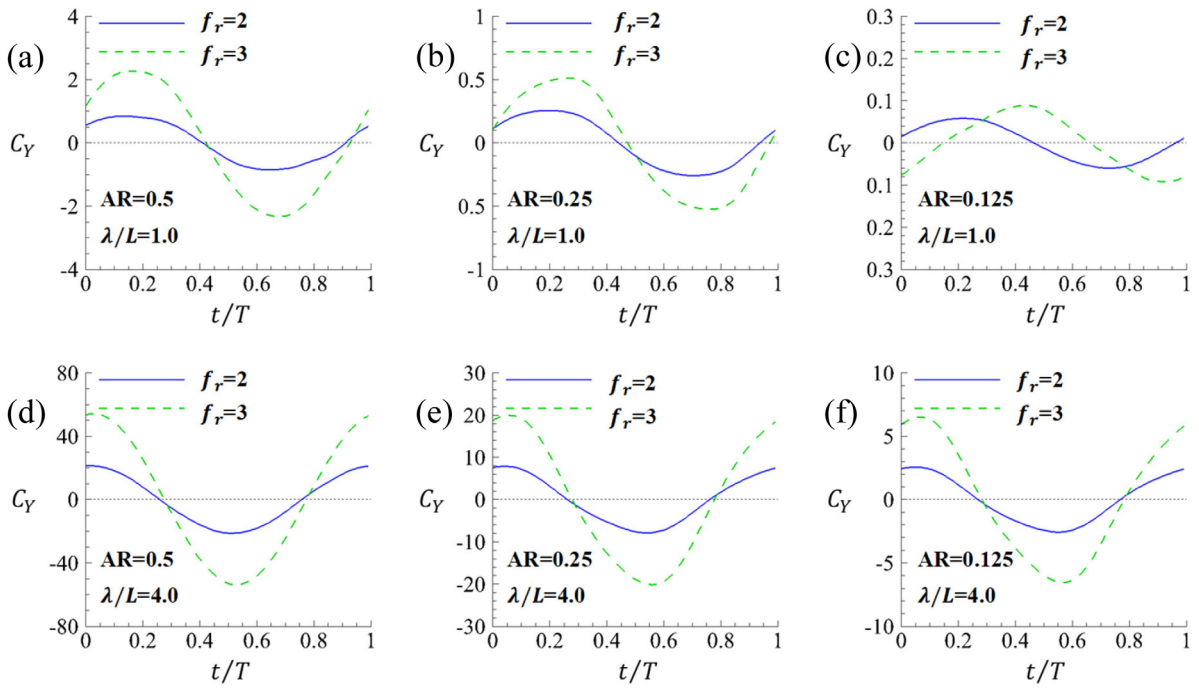

Fig. 9. Instantaneous vertical force coefficients within one motion period at various motion frequencies. (a–c) $\lambda/L = 1.0$, and (d–f) $\lambda/L = 4.0$. (a,d) $AR = 0.5$, and (b,e) $AR = 0.25$, and (c,f) $AR = 0.125$.

if the frequency is further increased. Besides, for most cases, the undulating fin obtains higher efficiency at $\lambda/L = 1.0$, especially at higher motion frequencies ($f_r > 2.0$). This result should be expected from the data presented in Fig. 5, where the amplitudes of the vertical force at $\lambda/L = 1.0$ are substantially smaller, indicating considerable reduction in

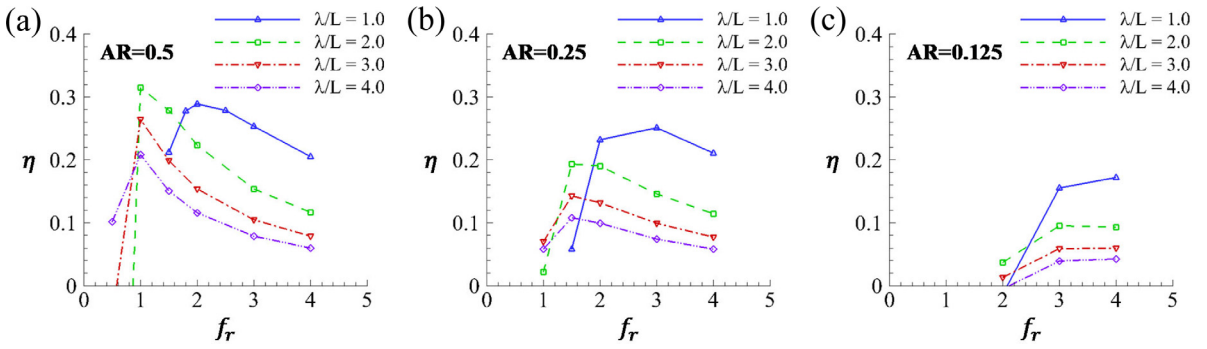

Fig. 10. Propulsive efficiencies as functions of reduced frequency at various wavelengths and aspect ratios. (a) $AR = 0.5$, and (b) $AR = 0.25$, and (c) $AR = 0.125$.

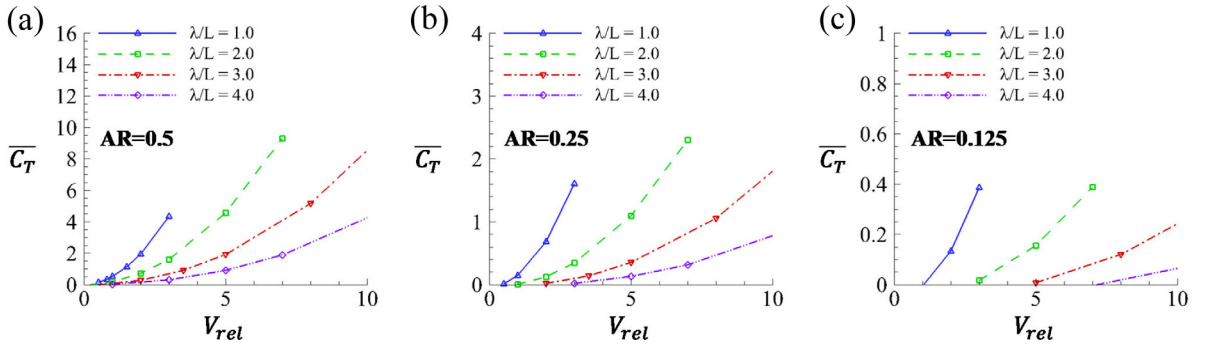

Fig. 11. Time averaged thrust coefficients as functions of relative velocity (V_{rel}) at various wavelengths and aspect ratios. (a) $AR = 0.5$, and (b) $AR = 0.25$, and (c) $AR = 0.125$.

power expenditure. At higher reduced frequencies, the propulsive efficiency declines as the increase of the wavelength. Exceptions are those cases at low motion frequencies, where the efficiency at $\lambda/L = 1.0$ drops most dramatically and the best performance is accomplished by the fin with $\lambda/L = 2.0$. The significant drop in efficiency can also be observed for other wavelengths at lower frequencies. The dramatic decrease in efficiency for the fin with $\lambda/L = 1.0$ occurs at relatively higher reduced efficiencies as it needs a higher frequency to produce net thrust force, which can be seen from Fig. 5(a–c).

Another indicator of the swimming efficiency is the wave efficiency, which can be defined as (Neveln et al., 2014):

$$\eta_{wave} = \frac{U_{sp}}{U_{wave}}, \tag{26}$$

where U_{sp} is the self-propelled speed and $U_{wave} = f\lambda$ is the wave speed. As the undulating fin in the present study is not swimming freely, the value of U_{sp} is not available. However, as demonstrated in Fig. 11, for all three aspect ratios, shorter wavelengths create higher thrust force at the same relative velocity V_{rel}, indicating higher wave efficiencies. The best wave efficiency is accomplished at $\lambda/L = 1.0$, which agrees with the findings from Fig. 10 that the undulating fin achieves the highest hydrodynamic efficiency at $\lambda/L = 1.0$.

4.2. Propulsive performance near the ground

In this section, the propulsive performance of the undulating pectoral fin in different proximities to the ground is analyzed and compared with those cases without ground effect.

4.2.1. Ground effect on hydrodynamic forces

Fig. 12(a–c) compare the thrust coefficients of the undulating fin as functions of wavelength at different proximities to the ground and various aspect ratios. It is seen that the thrust coefficients are declined for most cases due to the presence of the ground effect. The present finding shows difference from previous studies on the flapping foils where it was found that the thrust force or swimming speed can be enhanced due to the presence of the ground effect (Fernández-prats et al., 2015; Quinn et al., 2014a; Park et al., 2017; Zhang et al., 2017). This is not surprising because the kinematics of the present pectoral fin is significantly different from the flapping foils and the deformation of the fin is fully three-dimensional whereas only two-dimensional deformation was occurred for the flapping foils in previous papers. Besides,

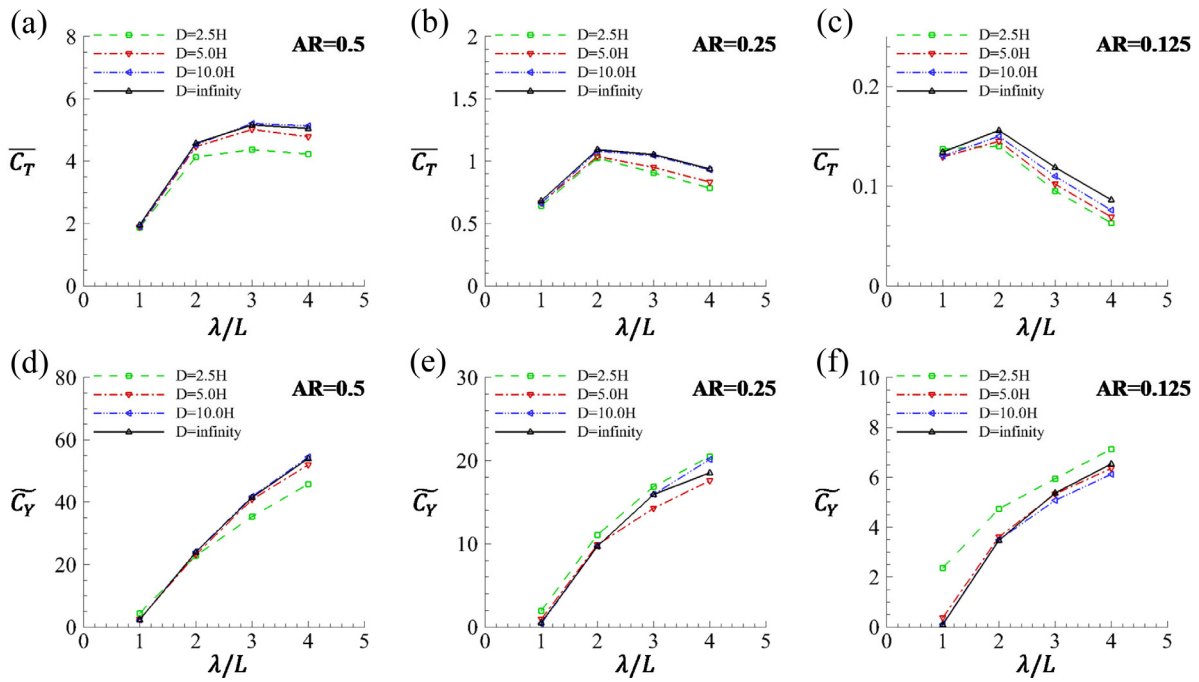

Fig. 12. Mean thrust coefficients (a–c) and amplitudes of vertical force coefficients (d–f) as functions of wavelength at various distances to the ground. $f_r = 3.0$. (a,d) $AR = 0.5$, and (b,e) $AR = 0.25$, and (c,f) $AR = 0.125$.

an experimental study of Blevins and Lauder (2013) also concluded that the ground effect does not necessarily enhance the propulsive performance of an undulating fin.

It can also be observed from Fig. 12(a–c) that the ground effect on the thrust generation becomes more pronounced at longer wavelengths. Besides, for all three aspect ratios, the differences of thrust coefficient between various proximities to the ground are marginal at $\lambda/L = 1.0$. In terms of the amplitudes of vertical force, it is observed from Fig. 12(d) that for an undulating fin with a larger aspect ratio, $\widetilde{C_Y}$ increases slightly at shorter wavelengths due to the ground effect while decreasing more considerably for longer wavelengths. With the decrease of aspect ratio, the variation of $\widetilde{C_Y}$ with the proximity to the ground becomes nonlinear. For the smallest proximity ($D = 2.5\ H$), the amplitudes of the vertical force become higher due to the ground effect. As aforementioned, the motions with longer wavelengths (e.g., $\lambda/L = 4.0$) are often considered as flapping instead of undulating. Therefore, the results demonstrated in Fig. 12 also indicate that the time-averaged thrust of flapping motion is more influenced by the ground effect, especially for larger aspect ratio cases.

Fig. 13 plots the time histories of thrust coefficients in the presence of the ground effect at $f_r = 3.0$. It is seen that the thrust coefficient profiles are sinusoidal for both wavelengths if there is no ground effect. When the ground effect is introduced and for larger proximities, the existence of the bottom wall modifies the magnitudes of peaks and troughs and leads to slight phase shifting while the overall patterns remain similar. However, for cases with the closest proximity, the thrust force profile is remarkably changed by the ground effect, especially for shorter wavelengths and smaller aspect ratios. Specifically, the thrust coefficient profiles become non-sinusoidal with multiple more significant peaks and troughs. Moreover, the instantaneous thrust coefficient curve shows asymmetry between the first and second half of the motion period. Nevertheless, the time-averaged thrust force at $\lambda/L = 1.0$ is less affected compared with that of $\lambda/L = 4.0$ as observed from Fig. 12(a–c).

The time histories of vertical force coefficients with the ground effect at $f_r = 3.0$ are demonstrated in Fig. 14. Similar to the thrust coefficient, with the decrease of the distance to the bottom wall, the variation of the vertical force becomes non-harmonic. The alteration of the vertical force history due to the ground effect is more remarkable for shorter wavelengths and smaller aspect ratios. Furthermore, the mean vertical force is no longer zero due to the presence of the ground effect as demonstrated in Fig. 15. As the decrease of the distance to the ground and the increase of the wavelength, the mean vertical forces become larger. Moreover, for most cases considered here (except those when $AR = 0.5$ and $D = 5.0H$, $10H$ and ∞), the mean vertical forces generated by the undulating fin are negative, indicating the vertical force pulls the fin towards the ground. This is a reminiscent of previous study of Quinn et al. (2014b), where it was found that the lift production of a pitching foil in the presence of the ground effect was divided into two regimes: (1) the foil was pulled towards the wall when the distance was between 0.4 to 1.0 chord length; (2) the foil was pushed away from the ground when the distance was 0.25 to 0.4 chord length. However, only the behavior in the first regime is observed for the

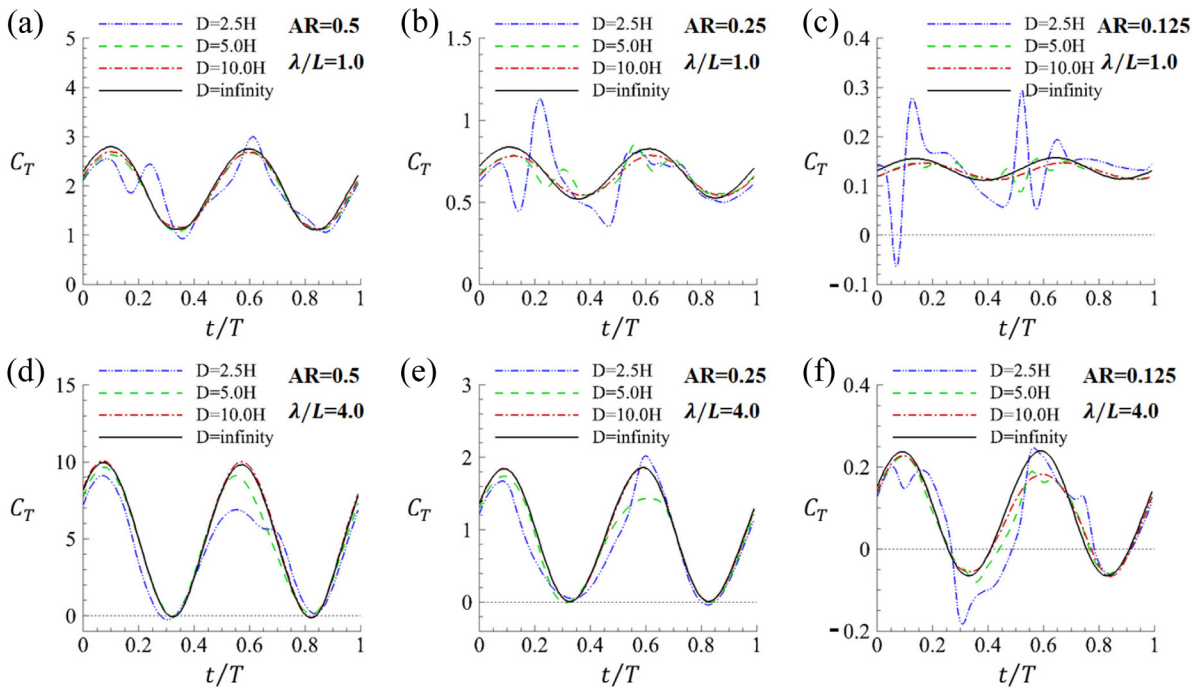

Fig. 13. Instantaneous thrust coefficients within one motion period at various distances to the ground. $f_r = 3.0$. (a–c) $\lambda/L = 1.0$, and (d–f) $\lambda/L = 4.0$. (a,d) $AR = 0.5$, and (b,e) $AR = 0.25$, and (c,f) $AR = 0.125$.

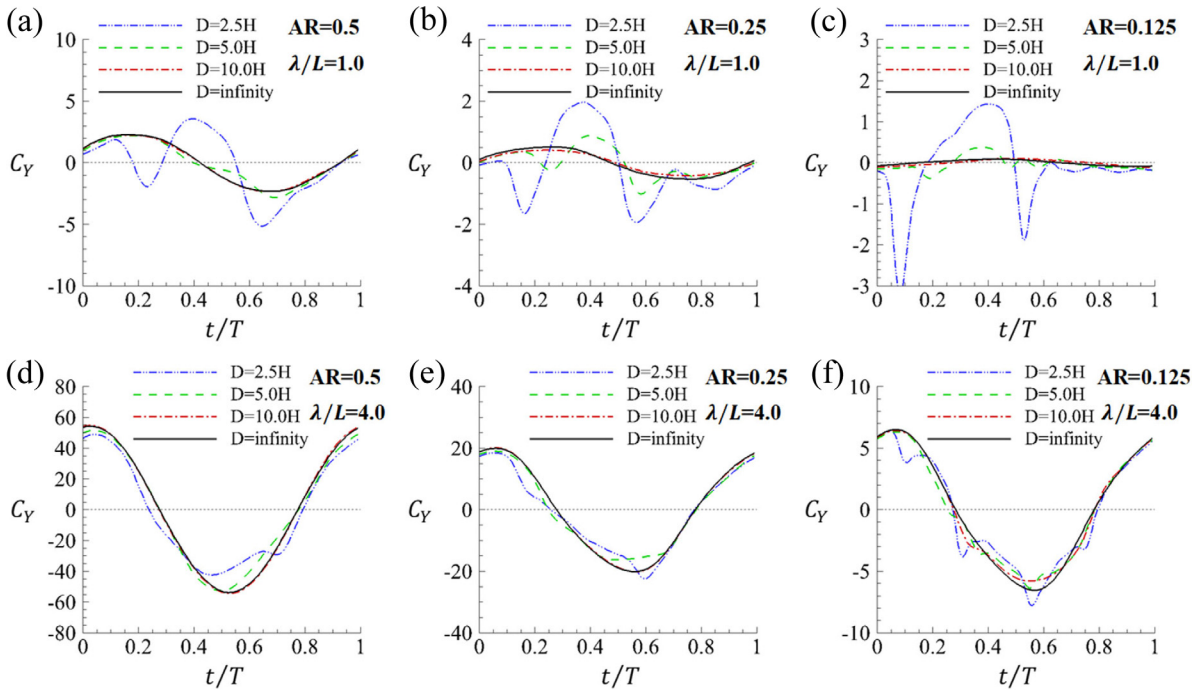

Fig. 14. Instantaneous vertical force coefficients within one motion period at various distances to the ground. $f_r = 3.0$. (a–c) $\lambda/L = 1.0$, and (d–f) $\lambda/L = 4.0$. (a,d) $AR = 0.5$, and (b,e) $AR = 0.25$, and (c,f) $AR = 0.125$.

proximities considered in the present work due to the significant different kinematics between an undulating fin and a rigid pitching foil. It is also noted that the fin with $AR = 0.5$ produces non-zero mean vertical forces at larger wavelengths when the ground effect is not present, which can be attributed to the accumulation of numerical errors. However, the

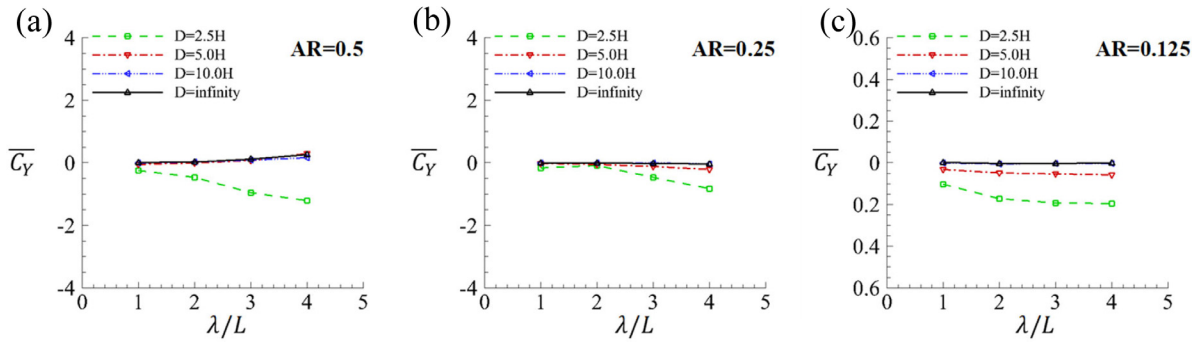

Fig. 15. Mean vertical force coefficients as functions of wavelength at various distances to the ground. $f_r = 3.0$. (a) $AR = 0.5$, and (b) $AR = 0.25$, and (c) $AR = 0.125$.

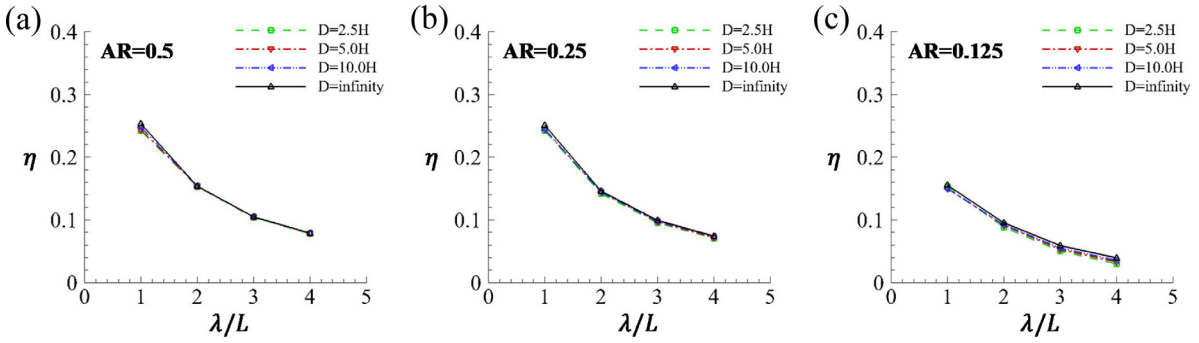

Fig. 16. Propulsive efficiencies as functions of wavelength at various distances to the ground. $f_r = 3.0$. (a) $AR = 0.5$, and (b) $AR = 0.25$, and (c) $AR = 0.125$.

deviation should be considered as marginal, especially when compared with the amplitude of the instantaneous vertical force curve shown in Fig. 14(d).

4.2.2. Ground effect on propulsive efficiency

Fig. 16 demonstrates the propulsion efficiencies of the undulating pectoral fins under the ground effect at $f_r = 3.0$. It is observed that for all aspect ratios and distances to the ground, the efficiency declines as the increase of the wavelength. Additionally, at $f_r = 3.0$, the propulsion efficiency at all three aspect ratios remains little changed by the presence of the ground. Compared with the ground effect on the force creation shown in Fig. 12, the influence on the propulsive efficiency is much smaller. This agrees with some previous studies on the flapping foils in the presence of ground effect, where it was found that the efficiency of the flapping panel remained relatively constant despite the changes of hydrodynamic forces (Quinn et al., 2014b,a).

4.3. Near-fin vorticity fields

Vorticity fields around the undulating fin without the ground effect are firstly demonstrated in this section. The influence of the presence of the bottom wall on the flow fields will be discussed in Section 4.4.

Fig. 17 shows the vorticity contours within the plane $z = 0.8W$ for two different wavelengths ($\lambda/L = 1.0$ and 4.0) without the ground effect. It is observed that for both wavelengths, vortices with opposite rotations are shed off from the trailing edge of the fin, forming a classic reversed Von Karman street, which is similar to the observation of Neveln et al. (2014). A comparison of Fig. 17(a) and (b) reveals that the trailing edge vortex created at the longer wavelength is much stronger and the interaction between the shed clockwise and counter-clockwise vortices is more significant. Moreover, the fin with $\lambda/L = 4.0$ generates clear leading edge vortices, which will separate from the fin, leading significant pressure difference between the two sides of the fin. The simultaneous creation of the leading and trailing edge vortices is also widely observed in many previous studies on flapping wings (Gursul and Cleaver, 2018; Shi et al., 2020a). In contrast, no obvious leading edge vortex is generated by the fin with the shorter wavelength. However, flow separations can also be noticed near the leading edge and at the crests and troughs of the fin surface. Since the flow separation is less significant for shorter wavelengths, the pressure force acting on the fin surface can be considerably reduced, leading to a reduction in thrust, as observed in Fig. 5 (a).

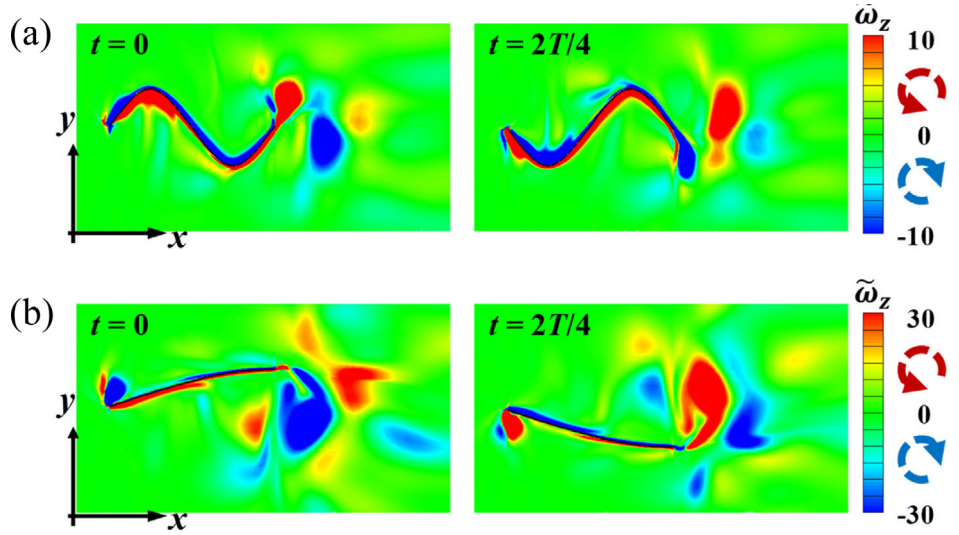

Fig. 17. Vorticity contours within $z = 0.8W$ plane without ground effect at $AR = 0.5$ and $f_r = 3.0$. (a) $\lambda/L = 1.0$ and (b) $\lambda/L = 4.0$.

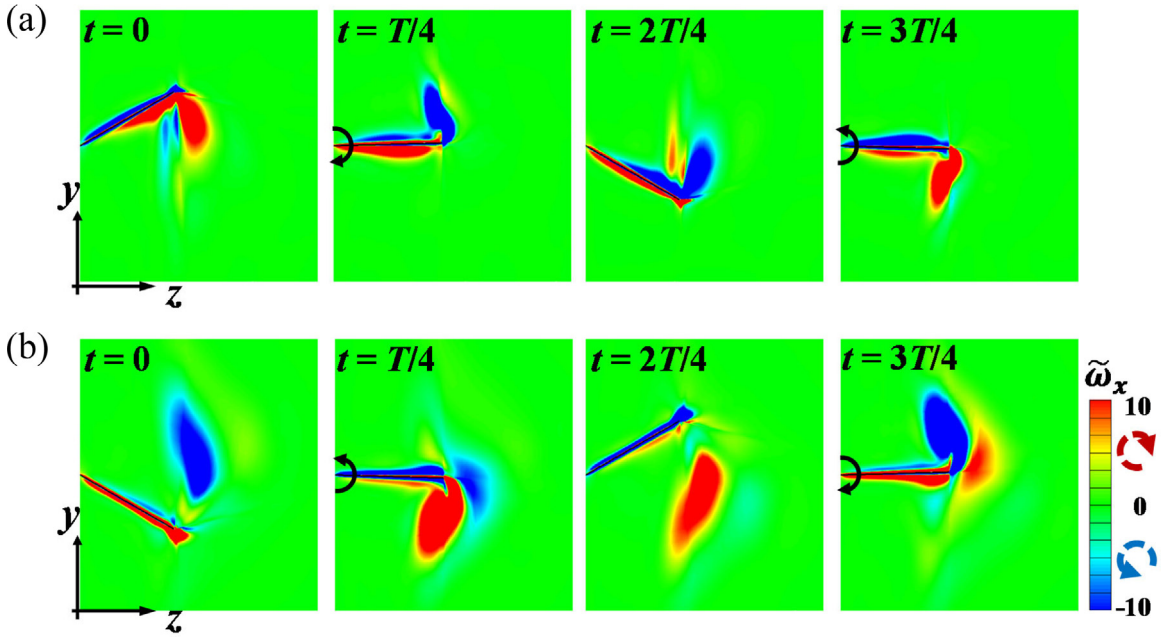

Fig. 18. Vorticity contours within $x = 0.25L$ (a) and $x = 0.75L$ (b) planes without the ground effect at $\lambda/L = 1.0$, AR = 0.5 and $f_r = 3.0$. The black solid arrows indicate the pitch direction of the ray.

Fig. 18 demonstrates the vorticity contours within transverse planes $x = 0.25L$ and $x = 0.75L$ of the fin at $\lambda/L = 1.0$. The anterior ($x = 0.25L$) and posterior ($x = 0.75L$) rays are out of phase with each other and as the fin rays oscillate within these planes, it is clear that vortices with similar strength to the trailing edge vortices illustrated in Fig. 17(a) are shed off from the tip of the rays and counter-rotating vortices are created when the ray changes its moving direction. Additionally, the strength of these vortices increases for more downstream planes, i.e., the vorticity within plane $x = 0.75L$ is stronger than that of plane $x = 0.25L$. The same contours for the fin with a longer wavelength ($\lambda/L = 4.0$) are plotted in Fig. 19, where the anterior and posterior rays are in-phase with each other. Similar to the fin with shorter wavelength, counter-rotating vortices are shed off with the oscillation of the ray and the vortex strength within the posterior plane is stronger than those within the upstream plane. Moreover, the vortices shed off from the anterior and posterior rays rotate in the same direction when $\lambda/L = 4.0$ while those generated by the fin with $\lambda/L = 1.0$ (see Fig. 18) are of opposite rotating directions.

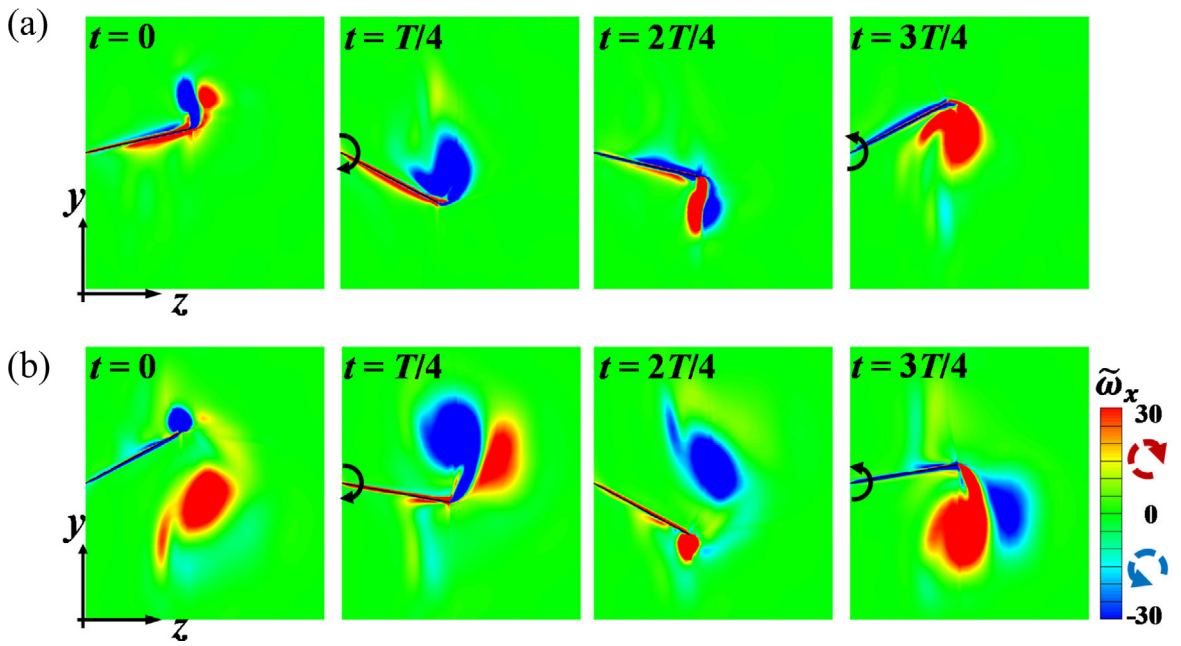

Fig. 19. Vorticity contours within $x = 0.25L$ (a) and $x = 0.75L$ (b) planes without the ground effect at $\lambda/L = 4.0$, AR = 0.5 and $f_r = 3.0$. The black solid arrows indicate the pitch direction of the ray.

Table 4
Time-averaged thrust coefficients in the ground effect at $f_r = 3.0$.

λ/L	AR	$\overline{C_T}$		
		$D = \infty$	$D = 2.5H$	Difference
1.0	0.500	1.952	1.869	−4.3%
	0.250	0.681	0.641	−5.9%
	0.125	0.134	0.137	2.2%
4.0	0.500	5.047	4.225	−16.3%
	0.250	0.938	0.785	−16.3%
	0.125	0.086	0.063	−26.7%

4.4. Discussions

4.4.1. On the thrust generation in ground effect

As observed from Fig. 12(a–c) that the time-averaged thrust coefficients of the undulating fin are reduced due to the presence of the ground effect and the reduction is more significant for longer wavelength cases. Table 4 quantifies the effects of the presence of the ground on the mean thrust coefficients of the fin with various wavelengths and aspect ratios. The decrease of $\overline{C_T}$ is less than 6% when $\lambda/L = 1.0$ whereas for a longer wavelength ($\lambda/L = 4.0$), the reduction of $\overline{C_T}$ can be up to 27%.

Fig. 20 illustrates the iso-surfaces of the vorticity magnitude around the fin with $\lambda/L = 1.0$ at $t = 3T/8$. It seen that the fin creates two inter-connected, counter-rotating side vortex tubes (SV1 and SV2) as the associated rays are moving in opposite directions, which has also been demonstrated in Fig. 18, where the motions of the anterior and posterior rays are out of phase. Besides, the generation of the trailing edge vortex tube (TV) can also be observed. This wake structure resembles the vortex shedding pattern of an elongated anal fin described by Neveln et al. (2014). With the presence of the bottom wall, the changes of SV1 and SV2 are subtle. But it is noticed that the trailing edge vertex tube disappears, indicating the vorticity strength is weakened due to the ground effect. Despite the differences in the iso-surfaces of the vorticity magnitude are subtle, the modifications to the flow fields by the bottom wall are considerable. Fig. 21 demonstrates the streamlines and pressure distribution within two transverse planes. The most obvious characteristic of the flow pattern with the presence of the ground effect is the creation of a counter-clock rotating vortex near the bottom wall. The vortex is generated when the fluid is entering the area underneath the fin and interacting with the bottom wall. Besides, due to the restriction of the ground, the vortices shed from the tip of the fin seem to be less developed, i.e., the strength is not as strong as those created by the fin with no ground effect.

Fig. 22 demonstrates the iso-surfaces of the vorticity magnitude around the fin with a longer wavelength. It is observed that the fin also creates inter-connected side vortex tubes similar to those shown in Fig. 20. However, with $\lambda/L = 4.0$,

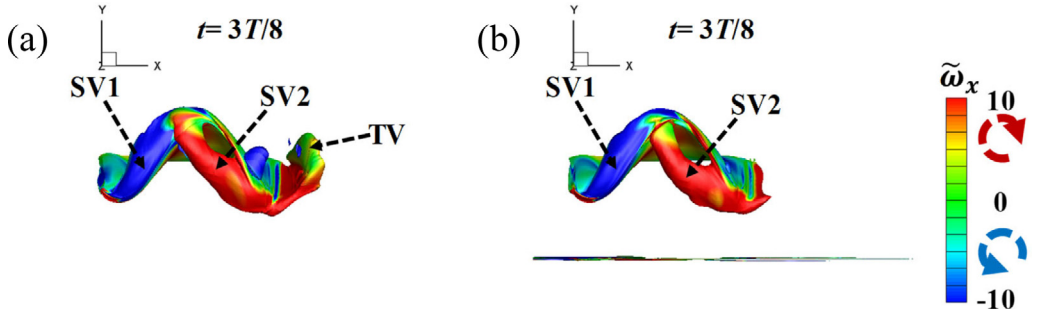

Fig. 20. The iso-surfaces of the vorticity magnitude ($\|\tilde{\omega}\| = 20$) at $\lambda/L = 1.0$, $AR = 0.5$ and $f_r = 3.0$. (a) Without the ground effect; (b) with the ground effect. The iso-surfaces are colored by x-vorticity. (For interpretation of the references to color in this figure legend, the reader is referred to the web version of this article.)

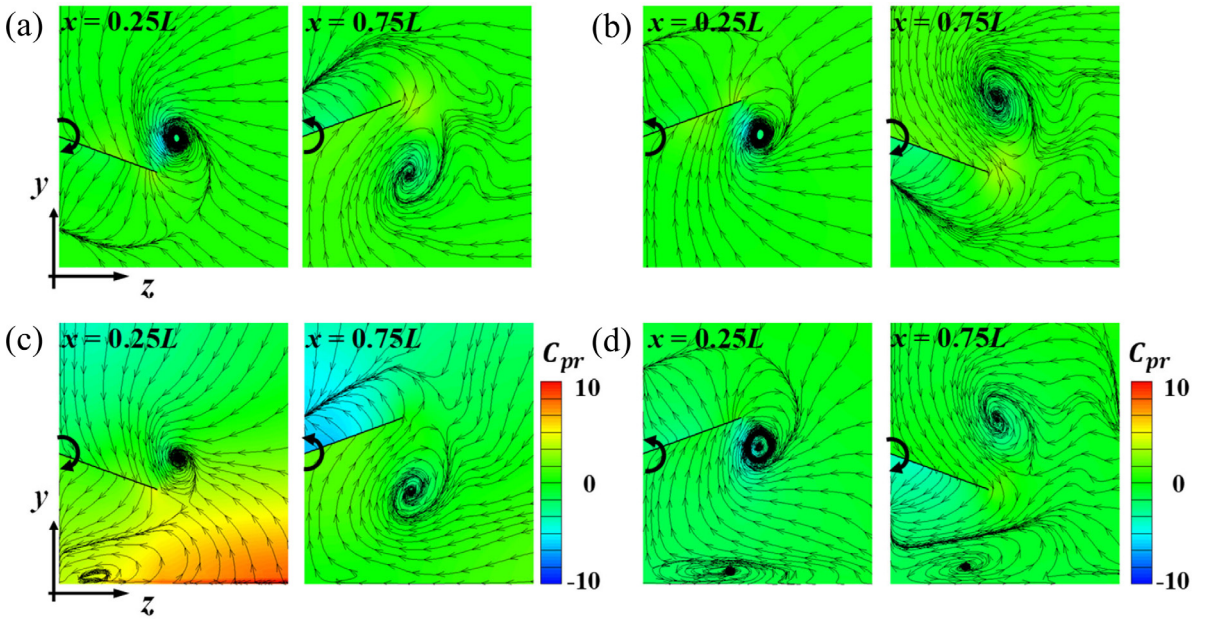

Fig. 21. The streamlines with the $x = 0.25L$ and $0.75L$ planes at $\lambda/L = 1.0$, $AR = 0.5$ and $f_r = 3.0$. (a,c) $t = 3T/8$; (b,d) $t = 7T/8$. (a–b) Without the ground effect; (c–d) with the ground effect. The contour shows the pressure coefficient distribution.

the phase lag between the leading and trailing edges is 90 degree, i.e., the anterior and posterior parts of the fin are in phase with each other for most time of the motion period. Thus, the successive side vortex starts to be formed when the former counter-rotating one is almost shed off. In contrast, the fin with $\lambda/L = 1.0$, vortices with opposite rotations are shed off simultaneously from the side edge of the fin (also be seen in Fig. 18). With the existence of the ground effect, the vortex tube shed by the side edge is noticeably shrunk and the oblique angle becomes smaller as illustrated in Fig. 22(c) and (d). The same iso-surfaces in Fig. 22 are colored by z-vorticity and viewed from a different perspective in Fig. 23. It is seen that the vortex tubes shed off from the side edge (SV) and trailing edge (TV) are inter-connected for the fin with no ground effect, as shown in Fig. 23(a) and (b). However, for the fin in the ground effect, the connection between SV and TV is broken, which can be clearly seen from Fig. 23(d). Moreover, the decrease of the strength of the trailing edge vortex is also significant, which will further decrease the thrust production.

Fig. 24 shows the flow fields and pressure distributions within $x = 0.25L$ and $0.75L$ planes at $t = T/8$ and $5T/8$. Similar to the observations from Fig. 21 that the interaction between the vortices shed off from the fin and the bottom wall leads to the creation of a counter-clock rotating vortex near the ground. The vortex is created during the down-stroke of the fin within $x = 0.25L$ ($t = T/8$) where the flow is compressed by the fin and the bottom wall. Besides, the near-wall vortex can also be generated during the up-stroke of the fin ($t = 5T/8$) when the flow is moving into the region under the fin. Additionally, the vortices shed off from the fin in the presence of the wall are considerably less strong as those without the ground effect. This has also been noticed in Fig. 22 where the vortices shed by the side and trailing edges shrink due to the ground effect. Furthermore, the alteration to the flow field also significantly change the pressure distribution.

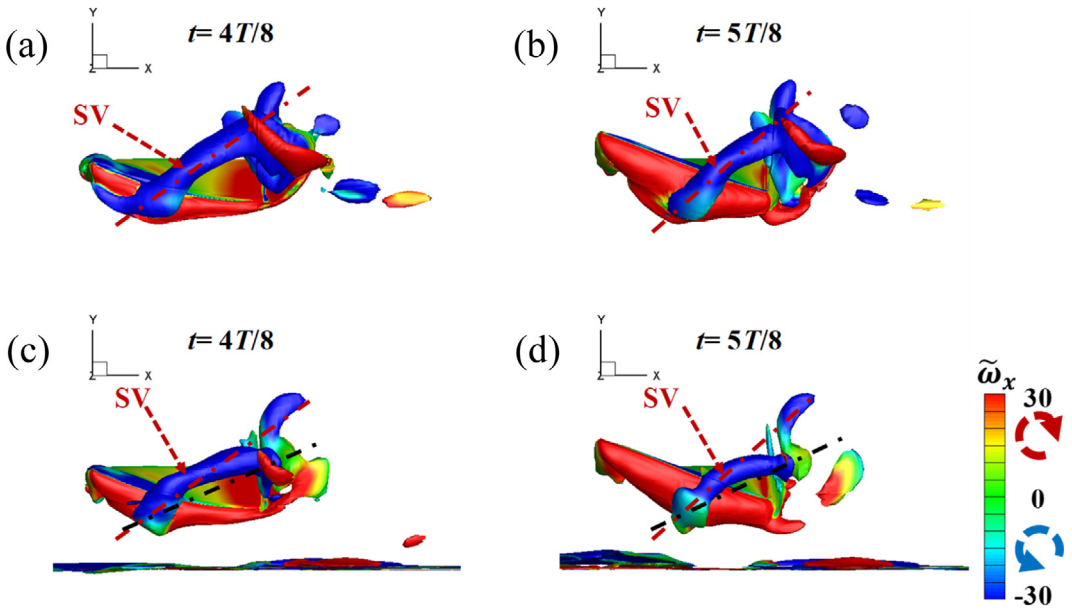

Fig. 22. The iso-surfaces of vorticity magnitude ($\|\tilde{\omega}\| = 50$) at $\lambda/L = 4.0$, $AR = 0.5$ and $f_r = 3.0$. (a–b) Without the ground effect, and (c–d) with the ground effect. The iso-surfaces are colored by x-vorticity. (For interpretation of the references to color in this figure legend, the reader is referred to the web version of this article.)

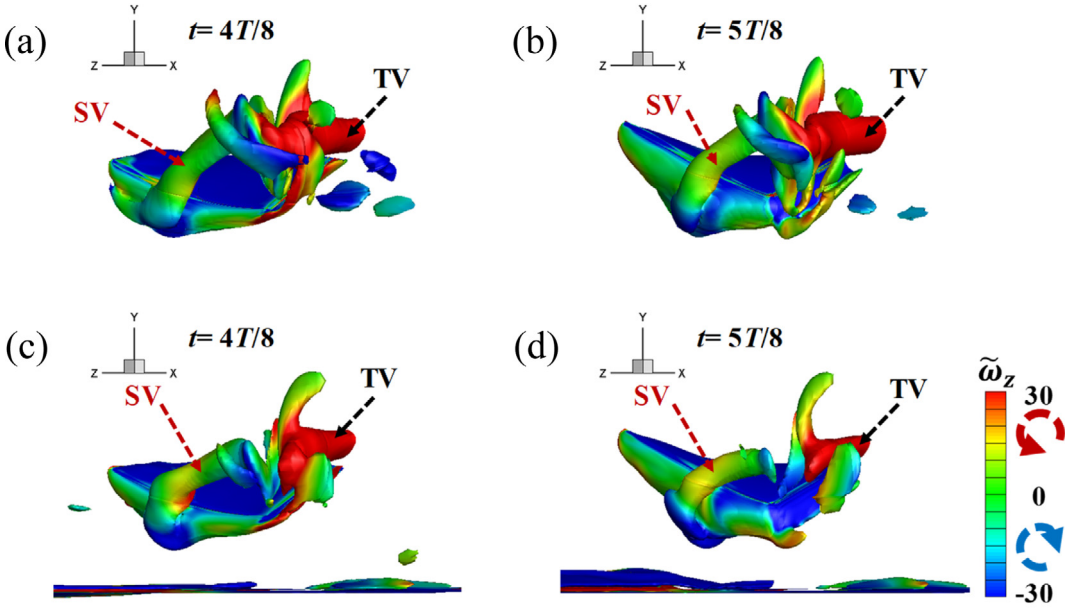

Fig. 23. The iso-surfaces of vorticity magnitude ($\|\tilde{\omega}\| = 50$) at $\lambda/L = 4.0$, $AR = 0.5$ and $f_r = 3.0$. (a–b) Without the ground effect, and (c–d) with the ground effect. The iso-surfaces are colored by z-vorticity. (For interpretation of the references to color in this figure legend, the reader is referred to the web version of this article.)

Specifically, the pressure difference between the two sides of the fin is reduced due to the ground effect, indicating the reduction in the generated lift force, which will further lead to a decrease in the thrust creation.

4.4.2. On the propulsive mechanisms

For fish locomotion, there are two basic thrust production mechanisms, namely: (1) the added-mass mechanism, where the thrust is produced by the reactive force from the accelerated adjacent fluid; and (2) the lift-based mechanism, where the thrust is generated by reorienting the lift force (which is accomplished by creating significant pressure

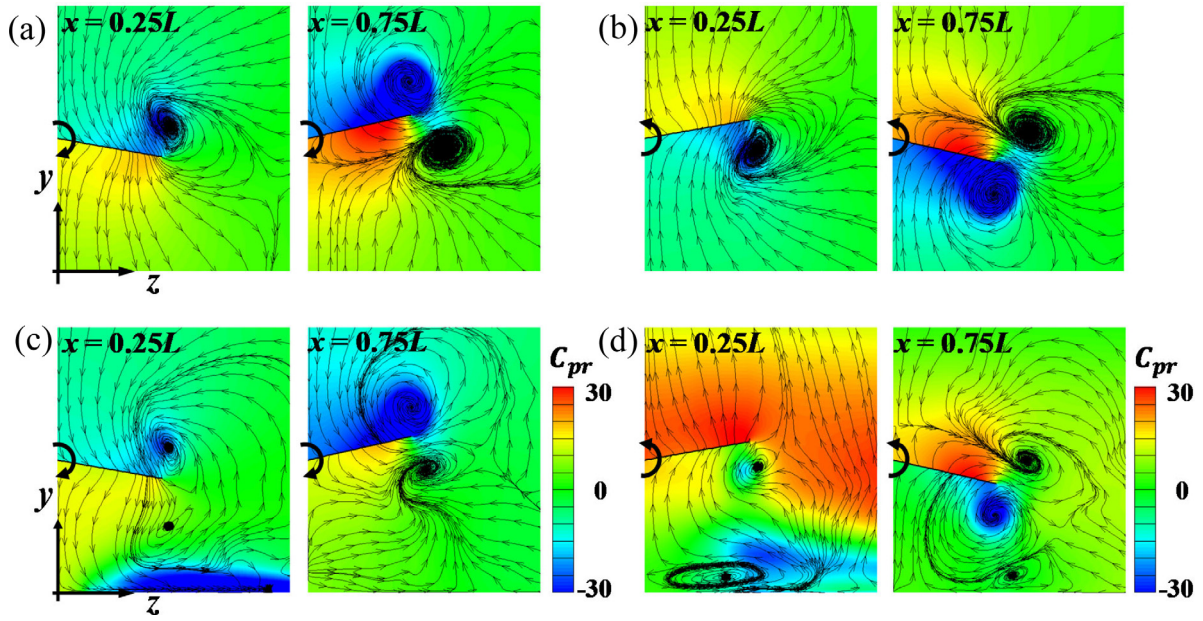

Fig. 24. The streamlines with the $x = 0.25L$ and $0.75L$ planes at $\lambda/L = 4.0$, $AR = 0.5$ and $f_r = 3.0$. (a, (c) $t = T/8$; (b,d) $t = 5T/8$. (a–b) Without the ground effect; (c–d) with the ground effect. The contour shows the pressure coefficient distribution.

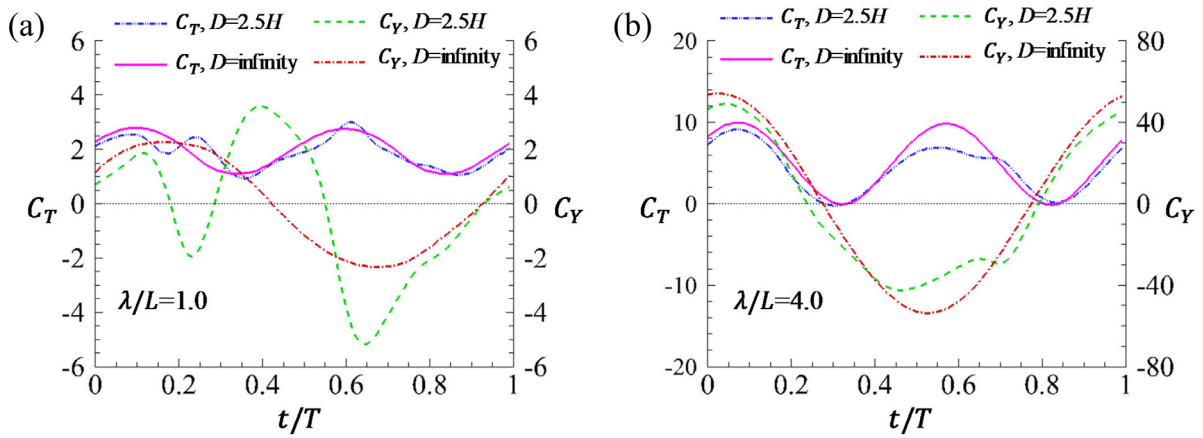

Fig. 25. Instantaneous thrust and vertical force coefficients of the fin with (a) $\lambda/L = 1.0$ and (b) $\lambda/L = 4.0$. $AR = 0.5$ and $f_r = 3.0$.

difference at the opposite sides of the body via manipulating the vortex shedding and vortex-body interaction) in the moving direction (Bottom II et al., 2016). Previous studies reveal that the added-mass mechanism is usually employed by undulatory swimmers while the oscillatory (flapping) fins can rely on both mechanisms for propulsion, depending on the motion frequency (Andro and Jacquin, 2009). Fig. 25 compares the instantaneous thrust and vertical force coefficients of the fin with $\lambda/L = 1.0$ and 4.0. It can be observed from Fig. 25(b) that there is a considerable reduction in the magnitude of vertical force between $t/T = 0.4$ and 0.7 due to the ground effect and this change of C_Y is also reflected in the C_T curve with a similar variation profile. However, for a shorter wavelength, the significant change of C_Y due to the ground effect is not reflected by the variation of C_T, especially at the instant of $t/T = 0.4$. The difference can be explained by the different propulsive mechanisms used for undulating (shorter wavelength) and flapping (longer wavelength) motions. The flapping fin ($\lambda/L = 4.0$) employs lift-based mechanism for thrust generation, i.e., when the vertical force becomes zero, the thrust force also reaches zero. In contrast, the undulating fin ($\lambda/L = 1.0$) mainly uses the added-mass mechanism for propulsion, i.e., when C_Y reaches zero, there is still finite thrust generated by the fin.

5. Conclusions

In the present study, we numerically investigated the propulsive performance of an undulating pectoral fin with various aspect ratios in and out of the presence of the ground effect. The flow field was simulated by solving the URANS equations using a finite volume method while the motion of the fin was prescribed as a sinusoidal wave. It was found that for higher aspect ratios, $\overline{C_T}$ was linear with the square of the normalized relative velocity and the inverse square of the wavelength ratio while for lower aspect ratios, $\overline{C_T}$ was linear with the cube of the normalized relative velocity and the inverse fourth power of the wavelength ratio. Additionally, the Strouhal number can only be used as a scaling parameter for the case of longer wavelengths. Moreover, the fin with $\lambda/L = 1.0$ produced the highest propulsive efficiency at higher frequencies while the efficiency was decreased dramatically at lower frequencies.

With the presence of the ground effect, the thrust generation was degraded for most cases while the propulsive efficiency remained relatively unchanged. Besides, the fin generated considerable mean vertical force with negative value, indicating the fin was pulled towards the ground. The variations of the fluid force were related with the creation of near-wall vortices, the weakened vortex shedding and the breaking of the inter-connection between the vortex tubes shed off from the side and the trailing edges. The present findings suggest that the undulating fin can reduce the ground effect and improve the propulsive efficiency by decreasing its wavelength. It is also worth pointing out that the ground effect is closely associated with the exact kinematics, thus the fin can adjust its kinematics other than increasing or decreasing the wavelength to change the interaction with the bottom wall. In the present work, the fin employs a sinusoidal wave form propagating in the same direction as the incoming flow. It is expected that non-harmonic kinematics may mitigate the reduction of mean thrust force or even be beneficial with the presence of the ground effect.

Declaration of competing interest

The authors declare that they have no known competing financial interests or personal relationships that could have appeared to influence the work reported in this paper.

References

Andro, J.Y., Jacquin, L., 2009. Frequency effects on the aerodynamic mechanisms of a heaving airfoil in a forward flight configuration. Aerosp. Sci. Technol. 13, 71–80. http://dx.doi.org/10.1016/j.ast.2008.05.001.

Blevins, E.L., Lauder, G.V., 2012. Rajiform locomotion: Three-dimensional kinematics of the pectoral fin surface during swimming in the freshwater stingray potamotrygon orbignyi. J. Exp. Biol. 215 (18), 3231–3241. http://dx.doi.org/10.1242/jeb.068981.

Blevins, E., Lauder, G.V., 2013. Swimming near the substrate: A simple robotic model of stingray locomotion. Bioinspir. Biomim. 8, 016005. http://dx.doi.org/10.1088/1748-3182/8/1/016005.

Bottom II, R.G., Borazjani, I., Blevins, E.L., Lauder, G.V., 2016. Hydrodynamics of swimming in stingrays: Numerical simulations and the role of the leading-edge vortex. J. Fluid Mech. 407–443. http://dx.doi.org/10.1017/jfm.2015.702.

Curet, O.M., Patankar, N.A., Lauder, G.V., Maciver, M.A., 2011a. Aquatic manoeuvering with counter-propagating waves: A novel locomotive strategy. J. R. Soc. Interface 8, 1041–1050.

Curet, O.M., Patankar, N.A., Lauder, G.V., MacIver, M.A., 2011b. Mechanical properties of a bio-inspired robotic knifefish with an undulatory propulsor. Bioinspir. Biomim. 6 (2), 026004. http://dx.doi.org/10.1088/1748-3182/6/2/026004.

Dai, L., He, G., Zhang, X., 2016. Self-propelled swimming of a flexible plunging foil near a solid wall. Bioinspir. Biomim. 11 (4), http://dx.doi.org/10.1088/1748-3190/11/4/046005.

Dai, H., Luo, H., de Sousa, P.J.S.A.F., Doyle, J.F., 2012. Thrust performance of a flexible low-aspect-ratio pitching plate. Phys. Fluids 24 (10), 1–9. http://dx.doi.org/10.1063/1.4764047.

Di Santo, V., Blevins, E.L., Lauder, G.V., 2017. Batoid locomotion: Effects of speed on pectoral fin deformation in the Little Skate, Leucoraja Erinacea. J. Exp. Biol. 220 (4), 705–712. http://dx.doi.org/10.1242/jeb.148767.

Di Santo, V., Kenaley, C.P., 2016. Skating by: Low energetic costs of swimming in a batoid fish. J. Exp. Biol. 219 (12), 1804–1807. http://dx.doi.org/10.1242/jeb.136358.

Dong, H., Bozkurttas, M., Mittal, R., Madden, P., Lauder, G.V., 2010. Computational modelling and analysis of the hydrodynamics of a highly deformable fish pectoral fin. J. Fluid Mech. 645, 345–373. http://dx.doi.org/10.1017/S0022112009992941.

English, I., Liu, H., Curet, O.M., 2019. Robotic device shows lack of momentum enhancement for gymnotiform swimmers. Bioinspir. Biomim. 14 (2), aaf983. http://dx.doi.org/10.1088/1748-3190/aaf983.

Fernández-prats, R., Raspa, V., Thiria, B., Huera-huarte, F., Godoy-diana, R., 2015. Large-amplitude undulatory swimming near a wall. Bioinspir. Biomim. 10, 016003. http://dx.doi.org/10.1088/1748-3190/10/1/016003.

Fish, F.E., Kolpas, A., Crossett, A., Dudas, M.A., Moored, K.W., Bart-Smith, H., 2018. Kinematics of swimming of the manta ray: Three-dimensional analysis of open-water maneuverability. J. Exp. Biol. 221 (6), http://dx.doi.org/10.1242/jeb.166041.

Gao, T., Lu, X., 2008. Insect normal hovering flight in ground effect. Phys. Fluids 20, 087101. http://dx.doi.org/10.1063/1.2958318.

Gursul, I., Cleaver, D., 2018. Plunging oscillations of airfoils and wings: Progress, opportunities, and challenges. AIAA J. 1–18. http://dx.doi.org/10.2514/1.J056655.

Heathcote, S., Wang, Z., Gursul, I., 2008. Effect of spanwise flexibility on flapping wing propulsion. J. Fluids Struct. 24 (2), 183–199. http://dx.doi.org/10.1016/j.jfluidstructs.2007.08.003.

Jameson, A., 1991. Time dependent calculations using multigrid, with applications to unsteady flows past airfoils and wings. In: AIAA 10th Computational Fluid Dynamics Conference. http://dx.doi.org/10.2514/6.1991-1596.

Jameson, A., Schmidt, W., Turkel, E.L.I., 1981. Numerical solution of the Euler equations by finite volume methods using runge kutta time stepping schemes. In: 14th Fluid and Plasma Dynamics Conference. http://dx.doi.org/10.2514/6.1981-1259.

Kim, H.S., Lee, J.Y., Chu, W.S., Ahn, S.H., 2017. Design and fabrication of soft morphing ray propulsor: Undulator and oscillator. Soft Robot. 4 (1), 49–60. http://dx.doi.org/10.1089/soro.2016.0033.

Kinsey, T., Dumas, G., 2012. Three-dimensional effects on an oscillating-foil hydrokinetic turbine. J. Fluids Eng. 134 (7), 071105. http://dx.doi.org/10.1115/1.4006914.

Lauder, G.V., 2015. Fish locomotion: Recent advances and new directions. Annual Rev. Mar. Sci. 7 (1), 521–545. http://dx.doi.org/10.1146/annurev-marine-010814-015614.
Liao, W., Cai, J., Tsai, H.M., 2007. A multigrid overset grid flow solver with implicit hole cutting method. Comput. Methods Appl. Mech. Engrg. 196 (1701), 9–12–1715. http://dx.doi.org/10.1016/j.cma.2006.09.012.
Liu, H., Curet, O.M., 2017. Propulsive performance of an under-actuated robotic ribbon fin. Bioinspiration Biomim. 12 (3), 36015. http://dx.doi.org/10.1088/1748-3190/aa7184.
Liu, F., Ji, S., 1996. Unsteady flow calculations with a multigrid Navier–Stokes method. AIAA J. 34 (10), 2047–2053. http://dx.doi.org/10.2514/3.13351.
Liu, G., Ren, Y., Zhu, J., Bart-Smith, H., Dong, H., 2015. Thrust producing mechanisms in ray-inspired underwater vehicle propulsion. Theor. Appl. Mech. Lett. 5 (1), 54–57. http://dx.doi.org/10.1016/j.taml.2014.12.004.
Liu, H., Taylor, B., Curet, O.M., 2017. Fin ray stiffness and fin morphology control ribbon-fin-based propulsion. Soft Robot. 4 (2), 103–116. http://dx.doi.org/10.1089/soro.2016.0040.
Liu, W., Xiao, Q., 2015. Investigation on darrieus type straight blade vertical axis wind turbine with flexible blade. Ocean Eng. 110, 339–356. http://dx.doi.org/10.1016/j.oceaneng.2015.10.027.
Liu, W., Xiao, Q., Zhu, Q., 2016. Passive flexibility effect on oscillating foil energy harvester. AIAA J. 54 (4), 1172–1187. http://dx.doi.org/10.2514/1.J054205.
Low, K.H., 2009. Modelling and parametric study of modular undulating fin rays for fish robots. Mech. Mach. Theory 44 (3), 615–632. http://dx.doi.org/10.1016/j.mechmachtheory.2008.11.009.
Lua, K.B., Lu, H., Zhang, X.H., Lim, T.T., Yeo, K.S., 2016. Aerodynamics of two-dimensional flapping wings in tandem configuration. Phys. Fluids 28 (12), http://dx.doi.org/10.1063/1.4971859.
Luo, Y., Xiao, Q., Shi, G., Wen, L., Chen, D., Pan, G., 2020. A fluid–structure interaction solver for the study on a passively deformed fish fin with non-uniformly distributed stiffness. J. Fluids Struct. 92, 102778. http://dx.doi.org/10.1016/j.jfluidstructs.2019.102778.
Mivehchi, A., Dahl, J., Licht, S., 2016. Heaving and pitching oscillating foil propulsion in ground effect. J. Fluids Struct. 63, 174–187. http://dx.doi.org/10.1016/j.jfluidstructs.2016.03.007.
Neveln, I.D., Bale, R., Bhalla, A.P.S., Curet, O.M., Patankar, N.A., MacIver, M.A., 2014. Undulating fins produce off-axis thrust and flow structures. J. Exp. Biol. 217 (2), 201–213. http://dx.doi.org/10.1242/jeb.091520.
Park, S.G., Kim, B., Sung, H.J., 2017. Hydrodynamics of a self-propelled flexible fin near the ground. Phys. Fluids 29, 051902. http://dx.doi.org/10.1063/1.4983723.
Perkins, M., Elles, D., Badlissi, G., Mivehchi, A., Dahl, J., Licht, S., 2018. Rolling and pitching oscillating foil propulsion in ground effect. Bioinspir. Biomim. 13, 016003.
Quinn, D.B., Lauder, G.V., Smits, A.J., 2014a. Flexible propulsors in ground effect. Bioinspir. Biomim. 9, 036008. http://dx.doi.org/10.1088/1748-3182/9/3/036008.
Quinn, D.B., Moored, K.W., Dewey, P.A., Smits, A.J., 2014b. Unsteady propulsion near a solid boundary. J. Fluid Mech. 742, 152–170. http://dx.doi.org/10.1017/jfm.2013.659.
Rosenberger, L.J., 2001. Pectoral fin locomotion in batoid fishes: Undulation versus oscillation. J. Exp. Biol. 204 (2), 379–394.
Salazar, R., Fuentes, V., Abdelkefi, A., 2018. Classification of biological and bioinspired aquatic systems: A review. Ocean Eng. 148, 75–114. http://dx.doi.org/10.1016/j.oceaneng.2017.11.012.
Sfakiotakis, M., Lane, D.M., Davies, J.B.C., 1999. Review of fish swimming modes for aquatic locomotion. IEEE J. Ocean. Eng. 24 (2), 237–252.
Shi, G., Xiao, Q., 2021. Numerical investigation of a bio-inspired underwater robot with skeleton-reinforced undulating fins. Eur. J. Mech. B/Fluids 87, 75–91. http://dx.doi.org/10.1016/j.euromechflu.2020.12.009.
Shi, G., Xiao, Q., Zhu, Q., 2020a. Effects of time-varying flexibility on the propulsion performance of a flapping foil. Phys. Fluids 32 (12), 121904. http://dx.doi.org/10.1063/5.0027927.
Shi, G., Xiao, Q., Zhu, Q., 2020b. Numerical investigation of an actively and passively controlled skeleton-reinforced caudal fin. AIAA J. 58 (11), 4644–4658. http://dx.doi.org/10.2514/1.j059141.
Shi, G., Xiao, Q., Zhu, Q., Liao, W., 2019. Fluid-structure interaction modeling on a 3D ray-strengthened caudal fin. Bioinspiration Biomim. 14, 036012. http://dx.doi.org/10.1088/1748-3190/ab0fbe.
Shirgaonkar, A.A., Curet, O.M., Patankar, N.A., MacIver, M.A., 2008. The hydrodynamics of ribbon-fin propulsion during impulsive motion. J. Exp. Biol. 211 (21), 3490–3503. http://dx.doi.org/10.1242/jeb.019224.
Tangorra, J.L., Davidson, S.N., Hunter, I.W., Madden, P.G.A., Lauder, G.V., Dong, H., Bozkurttas, M., Mittal, R., 2007. The development of a biologically inspired propulsor for unmanned underwater vehicles. IEEE J. Ocean. Eng. 32 (3), 533–550. http://dx.doi.org/10.1109/JOE.2007.903362.
Taylor, Z.J., Liberzon, A., Gurka, R., Holzman, R., Reesbeck, T., Diez, F.J., 2013. Experiments on the vortex wake of a swimming knifefish. Exp. Fluids 54 (8), 54–57. http://dx.doi.org/10.1007/s00348-013-1588-1.
Tsai, H.M., F. Wong, A.S., Cai, J., Zhu, Y., Liu, F., 2001. Unsteady flow calculations with a parallel multiblock moving mesh algorithm. AIAA J. 39 (6), 1021–1029. http://dx.doi.org/10.2514/2.1442.
Wang, Y., Tan, J., Zhao, D., 2015. Design and experiment on a biomimetic robotic fish inspired by freshwater stingray. J. Bionic Eng. 12 (2), 204–216. http://dx.doi.org/10.1016/S1672-6529(14)60113-X.
Xiao, Q., Liao, W., 2010. Numerical investigation of angle of attack profile on propulsion performance of an oscillating foil. Comput. & Fluids 39 (8), 1366–1380. http://dx.doi.org/10.1016/j.compfluid.2010.04.006.
Youngerman, E.D., Flammang, B.E., Lauder, G.V., 2014. Locomotion of free-swimming ghost knifefish: Anal fin kinematics during four behaviors. Zoology 117 (5), 337–348. http://dx.doi.org/10.1016/j.zool.2014.04.004.
Zhang, J., Bai, Y., Zhai, S., Gao, D., 2019. Numerical study on vortex structure of undulating fins in stationary water. Ocean Eng. 187 (June), 106166. http://dx.doi.org/10.1016/j.oceaneng.2019.106166.
Zhang, C., Huang, H., Lu, X., 2017. Free locomotion of a flexible plate near the ground. Phys. Fluids 29, 041903. http://dx.doi.org/10.1063/1.4981778.
Zhang, Y., Wang, S., Wang, X., Geng, Y., 2018. Design and control of bionic manta ray robot with flexible pectoral fin. In: IEEE International Conference on Control and Automation, ICCA, 2018-June. pp. 1034–1039. http://dx.doi.org/10.1109/ICCA.2018.8444283.
Zhao, Z., Dou, L., 2019. Computational research on a combined undulating-motion pattern considering undulations of both the ribbon fin and fish body. Ocean Eng. 183 (April), 1–10. http://dx.doi.org/10.1016/j.oceaneng.2019.04.094.
Zhou, C., Low, K.H., 2010. Better endurance and load capacity: An improved design of manta ray robot (roman-II). J. Bionic Eng. 7, S137–S144. http://dx.doi.org/10.1016/S1672-6529(09)60227-4.